Supporting information

Interfacial water mediated oxide path mechanism for efficient acidic water oxidation on Co_3O_4

Juan Zhu,[a†] Zhichang Liao,[a†] Shinuo Liu,[a]Jingxiang Xia,[a] Hongnan Jia[b] and Wei Luo[,a]*

[a]*College of Chemistry and Molecular Sciences, Wuhan University Wuhan, Hubei 430072, P. R. China*

[b]*College of Chemistry, Zhengzhou University, Zhengzhou, Henan 450001, P. R. China*

[*]Email: wluo@whu.edu.cn (W.L.)

Chemicals and Material Synthesis

Chemicals.

All reagents are of analytical grade and used without purification. Cobalt acetate tetrahydrate ($Co(CH_3COO)_2{\cdot}4H_2O$, Sinopharm Chemical Reagent), antimony trichloride($SbCl_3$, Aladdin Industrial,~99%), ethylene glycol($C_2H_6O_2$,Sinopharm Chemical Reagent), sulfuric acid (H_2SO_4, Sinopharm Chemical Reagent, 95.0 ~ 98.0%), hydrogen peroxide (H_2O_2, Sinopharm Chemical Reagent, ~ 30.0%), hydrochloric acid (HCl, Sinopharm Chemical Reagent, 36.0 ~ 38.0%), perchloric acid ($HClO_4$, Sinopharm Chemical Reagent, 70.0 ~ 72.0%), acetone (Sinopharm Chemical Reagent, ≥ 97%), commercial RuO_2 (Changcheng Chemical, > 99%), Nafion 115 solution (Sigma-Aldrich, ~ 5% in a mixture of lower aliphatic alcohols and water), absolute ethanol (Sinopharm Chemical Reagent, ≥ 99.7%), isopropanol (Sinopharm Chemical Reagent, ≥ 99.7%), The ultrapure water (18.25 MΩ cm^{-1}) prepared from an up water purification system was used throughout the whole experiment.

Synthesis of Co_3O_4, $Sb_{0.4}Co_{2.6}O_4$, $Sb_{0.3}Co_{2.7}O_4$, and $Sb_{0.1}Co_{2.9}O_4$ nanoparticles.

0.7 mmol of $Co(CH_3COO)_2{\cdot}4H_2O$, 0.23 mmol of $SbCl_3$, 33 mg of carbon powder, and 50 mL of ethanol were added into a 100 mL round-bottom flask, and the mixture was stirred for 1 hour. Then the mixture was transferred into a 100 mL teflon-sealed autoclave and placed in an oven at 180℃ for reaction for 18 hours. After the autoclave naturally cooled to room temperature, the products were obtained by centrifugation and washed with absolute ethanol for 3 times. Finally, the obtained black product was dried at 60 °C and then calcined at 380 °C for 10 h to obtain the final product. Then, inductively coupled plasma-atomic emission spectroscopy (ICP-AES) was used to quantify the doping content of Sb in the catalysts (Table S1), and the samples were named according to their actual Sb content.

Materials characterization.

(1) Inductively coupled plasma atomic emission spectroscopy (ICP-AES)

ICP-AES was conducted on Agilent 5110. First, for the pretreatment of the catalyst before ICP-AES testing: 1) 3 mg of the catalyst (Co_3O_4, $Sb_{0.1}Co_{2.9}O_4$, $Sb_{0.3}Co_{2.7}O_4$ and $Sb_{0.4}Co_{2.6}O_4$) was precisely weighed and digested in aqua regia. 2) The mixture was then transferred into a 15 mL Teflon-sealed autoclave and heated in an oven at 180°C

for 24 hours. 3) After cooling to room temperature, the digested solution was diluted to a final volume of 50 mL in a volumetric flask. 4) The solution was allowed to stand for 24 hours to ensure complete dissolution of the catalyst, after which the resulting clear and transparent solution was subjected to ICP-AES analysis.

The analytical procedure consisted of the following steps: 1) Calibration curve construction. A series of standard solutions (containing Co, Sb) with concentrations spanning the expected sample range was prepared. Each standard solution was measured five times to establish the relationship between elemental concentration (x-axis) and corresponding emission intensity (y-axis). 2) Sample analysis. All electrolyte samples were analyzed in quintuplicate under identical instrumental conditions. The measured emission intensities for Co and Sb were correlated with the calibration curves to determine their respective concentrations.

(2) X-ray powder diffraction (XRD)

XRD patterns were obtained on a Rigaku Miniflex600 X-ray powder diffractometer equipped with a Cu Kα radiation source (λ = 0.154178 nm), operating at 40 kV and 15 mA. The sample was ground into a fine powder, evenly packed into the sample holder, and then scanned. All of the diffraction data were collected in a 2θ range from 10° to 80° at a scanning rate of 10° min^{-1}.

(3) Transmission electron microscopy (TEM)

A homogeneous dispersion was prepared by ultrasonication of 2 mg catalyst in 10 mL of anhydrous ethanol for 30 minutes. The resulting suspension was deposited onto an ultra-thin carbon support film and dried in ambient air for 2 hours to ensure complete solvent evaporation. The specimen-loaded support film was mounted in a TEM holder and transferred into the specimen chamber of a JEM-2100Plus transmission electron microscope. Following the establishment of stable high-vacuum conditions, TEM analysis was conducted at an accelerating voltage of 200 kV. Initial low-magnification imaging was performed to identify electron-transparent regions of uniform sample thickness. Subsequently, the magnification was adjusted appropriately to observe and acquire morphological images of the sample. Image processing and analysis were performed using GMS 3 software. Particle size distribution analysis was performed using ImageJ software. Diameters of at least 100 randomly selected particles from distinct regions were measured to determine the mean particle size and generate the corresponding size distribution histogram. Specifically, 134 nanoparticles of Co_3O_4 and 119 nanoparticles of $Sb_{0.3}Co_{2.7}O_4$ were analyzed. The particle size distribution histograms for both materials were fitted with a Gaussian function to obtain

their respective mean particle diameters.

(4) The Spherical aberration-corrected HAADF-STEM

A homogeneous dispersion was prepared by ultrasonically dispersing 2 mg of catalyst in 10 mL of anhydrous ethanol for 30 min. The resulting suspension was deposited onto an ultra-thin carbon support film (3 nm thickness) and air-dried for 2 h under ambient conditions to ensure complete solvent evaporation. The specimen-loaded support film was mounted in a FE-TEM holder and transferred into the specimen chamber of a spherical aberration-corrected field-emission transmission electron microscope (JEM-ARM200CF, JEOL Ltd.). Following achievement of stable high-vacuum conditions ($<5\times10^{-5}$ Pa), analysis commenced by first identifying an electron-transparent region with uniform thickness under low-magnification STEM imaging. The operational mode was subsequently switched to HAADF-STEM with activated drift correction (AutoCure™), and a single-frame reference image was acquired while optimizing probe current (80-120 pA) and dwell time (5-20 μs/pixel) to achieve a signal-to-noise ratio (SNR) > 8. Finally, synchronized elemental mapping was performed by enabling energy-dispersive X-ray spectroscopy (EDS) and initiating HAADF-EDS acquisition at 512×512 pixel resolution. The EDS mapping was acquired with a process time of 255.43 seconds, resulting in a dead time of approximately 1% and a live time of 251.65 seconds.

(5) Soft X-ray absorption spectroscopy (soft-XAS)

The X-ray magnetic circular dichroism (XMCD) measurements at the $L_{2,3}$-edge and O *K*-edge were performed at the soft X-ray magnetic circular dichroism beamline (BL12B-a) of the Hefei National Synchrotron Radiation Laboratory (NSRL). The prepared sample was fixed onto the sample holder using vacuum-compatible conductive adhesive or metal clips to ensure good electrical contact for total electron yield (TEY) mode measurements. The region of interest was positioned to the beam center using a three-dimensional manipulator. The beam spot size on the sample was approximately 1 mm (horizontal) * 0.5 mm (vertical). All spectra were collected at room temperature in the total electron yield (TEY) mode by monitoring the sample drain current. A magnetic field of up to ±1T, applied parallel to the incident X-ray beam direction, was used to magnetize the sample. Raw data were pre-processed using the beamline's dedicated software, including normalization to the incident photon flux (I_0), background subtraction, and spectral smoothing. The Co *L*-edge spectra were energy-calibrated using a Co foil as a standard reference, while the O *K*-edge spectra were calibrated using CuO as a reference for the energy zero. Further spectral analysis was performed using the Athena software package.

(6) X-ray absorption spectroscopy of Co K-edge

A homogeneous dispersion was prepared by ultrasonically dispersing 40 mg of the sample in 5 mL of anhydrous ethanol for 1 h. Subsequently, 80 μL of Nafion® solution (5 wt%) was added, followed by an additional 1 h of ultrasonication. The resulting dispersion was uniformly coated onto a 2 × 2 cm^2 carbon paper substrate and air-dried at ambient temperature. Co K-edge X-ray absorption spectroscopy (XAS) measurements were performed in transmission mode using a Rapid XAFS2M spectrometer (Anhui Absorption Spectroscopy Instruments Co., Ltd.) operated at 20 kV and 40 mA. A spherically bent crystal analyzer (SBCA) with a Si (533) crystal and 500 mm curvature radius was employed for Co detection. Prior to data collection, the Si (111) double-crystal monochromator was calibrated by adjustment to the Bragg angle θ. Energy calibration was subsequently conducted by inserting a cobalt foil reference behind the sample holder and confirming the first-derivative peak position of the Co absorption edge at 7709 eV. Finally, XAS spectra of the sample were acquired. The Co_2O_3 reference signal used in our study was obtained from a standard database.

In situ X-ray absorption spectroscopy (XAS) measurements were conducted using an electrochemical cell. The sample preparation procedure was consistent with that of ex situ tests. The sample was mounted as the working electrode in a custom-built in situ cell containing 0.5 mol/L H_2SO_4 electrolyte, with an Ag/AgCl reference electrode and a Pt wire counter electrode installed. A potentiostat applied constant potentials (1.3 V and 1.5 V vs. RHE) sequentially. At each potential, the system was allowed to stabilize for ≥60 s to ensure steady-state conditions before synchronously acquiring XAS signals. This protocol was iteratively repeated to collect *in situ* XAS data across distinct electrochemical states. The schematic diagram of in-situ testing is shown in Figure S43.

The obtained XAS data were processed in Athena (version 0.9.26) for background, pre-edge line and post-edge line calibrations. Then, the Fourier transformed fitting was carried out in Artemis (version 0.9.26). The k^3 weighting, k-range of 2-11 $Å^{-1}$ and R range of 1-~3.5 Å were used for the fitting of Co_3O_4; k-range of 3- 11 $Å^{-1}$ and R range of 1- ~3.5 Å were used for the fitting of $Sb_{0.3}Co_{2.7}O_4$. The four parameters, coordination number, bond length, Debye-Waller factor and E_0 shift (CN, R, ΔE_0) were fitted without any one fixed, the σ^2 was set. For Wavelet Transform analysis, the χ(k) exported from Athena was imported into the Hama Fortran code. The parameters were listed as follows: R range, 1-4 Å, k range, 0-15 $Å^{-1}$ for samples; k weight, 3; and Morlet function with κ=10, σ=1 was used as the mother wavelet to provide the overall distribution.

(7) X-ray photoelectron spectroscopy (XPS)

X-ray photoelectron spectroscopy (XPS) analyses were conducted using a Thermo Fisher Scientific ESCALAB 250Xi spectrometer. The dried powder sample was uniformly dispersed onto conductive carbon tape and secured on a sample holder to ensure flat surface contact, thereby minimizing charge accumulation. The sample was rapidly transferred to the load-lock chamber to limit air exposure and subsequently introduced into the analysis chamber, where ultra-high vacuum conditions (< 10^{-8} Pa) were established prior to measurements to mitigate gas-phase interference. For XPS characterization, a survey scan (0-1350 eV) was first acquired to identify all detectable elements, followed by high-resolution scans of target core levels with an energy step size of 0.05-0.1 eV.

(8) X-ray absorption spectroscopy of Sb K-edge

Sb *K*-edge XAFS analyses were performed with Si (111) crystal monochromators at the BL14W Beam line at the Shanghai Synchrotron Radiation Facility (SSRF) (Shanghai, China). Before the analysis at the beamline, samples were placed into aluminum sample holders and sealed using Kapton tape film. The XAFS spectra were recorded at room temperature using a 4-channel Silicon Drift Detector (SDD) Bruker 5040. Sb *K*-edge extended X-ray absorption fine structure (EXAFS) spectra were recorded in transmission mode. Negligible changes in the line shape and peak position of Sb *K*-edge XANES spectra were observed between two scans taken for a specific sample. The XAFS spectra of these standard samples were recorded in transmission mode. The spectra were processed and analyzed by the software code Athena.

(9) *In-situ* attenuated total reflectance surface-enhanced infrared absorption spectroscopy (ATR-SEIRAS)

In-situ attenuated total reflectance surface-enhanced infrared absorption spectroscopy (ATR-SEIRAS) was carried out with Bruker Invenio R, equipped with a liquid nitrogen-cooled detector. A homemade IR cell with a polished Si prism was employed as experimental apparatus. The polished Si prism was ultrasonically cleaned by acetone, ethanol, and ultrapure water, respectively, followed by a thin gold layer chemically deposited on the surface of the silicon prism to enhance conductivity and infrared signal sensitivity (Figure S47). Then, 190 μL of catalyst slurry with a concentration of 5 mg/mL was applied to the Au surface. This slurry was prepared by dispersing 3 mg of catalyst in 0.6 mL solvent of isopropyl alcohol containing 0.1 wt. % Nafion®, followed by a 30 min of sonication. The assembled working electrodes were placed in a three-electrode electrochemical system, where Hg/Hg_2Cl_2 served as the reference electrode, platinum tablet as the counter electrode, and Ar-saturated 0.5

M H_2SO_4 as the electrolyte for the OER reaction. All measurements were performed using Chronoamperometry (CA) to investigate OER reaction intermediates and interfacial water at the applied potential of 1.3 to 1.8 V versus RHE.

(10) *In situ* O^{18} isotope labeling differential electrochemical mass spectrometry (DEMS)

A homogeneous catalyst ink was prepared by ultrasonically dispersing 3 mg of catalyst in a solution containing 460 µL of H_2O, 500 µL of anhydrous ethanol, and 40 µL of Nafion® (5 wt%) for 30 min. Subsequently, 48 µL of the ink was drop-casted onto the gold membrane of an *in situ* DEMS cell. After solvent evaporation under ambient conditions, the catalyst-coated gold membrane was applied as the working electrode. The Pt wire and Ag/AgCl (saturated KCl solution) were applied as the counter electrode and reference electrode (Figure S49), respectively. Then, electrochemical labeling was performed in 0.5 M H_2SO_4 prepared with $H_2{}^{18}O$ solvent. Linear sweep voltammetry (LSV) was conducted from 1.2 to 1.9 V vs. RHE (scan rate: 5 mV s^{-1}) while monitoring oxygen evolution signals (m/z=32, 34, 36) via mass spectrometry coupled through a molecular sieve interface. This process electrochemically deposits ^{18}O isotopes specifically onto the catalyst surface. Subsequently, the cell and catalyst were thoroughly rinsed with $H_2{}^{16}O$ (≥10 cycles) to remove physically adsorbed $H_2{}^{18}O$. After air-drying, the cell was reassembled with fresh 0.5 M H_2SO_4 ($H_2{}^{16}O$ solvent). Identical LSV scans (1.2-1.9 V vs. RHE) were performed in $H_2{}^{16}O$-based electrolyte and evolved gases were analyzed in real-time to quantify isotopic oxygen products (m/z=32 for $^{16}O_2$, m/z = 36 for $^{18}O_2$, m/z = 34 for $^{16}O^{18}O$).

(11) Monitoring of Dissolved Metal Ions

The catalyst ink was prepared by ultrasonically dispersing 5 mg of catalyst in 1 mL of isopropanol containing 0.1 wt% Nafion®, followed by uniformly coating the resulting suspension onto a carbon cloth substrate (0.5 cm × 0.5 cm). Chronoamperometric stability tests were performed in 0.5 M H_2SO_4 electrolyte (100 mL) at a constant current density of 10 mA cm^{-2}. During testing, 10 mL aliquots of electrolyte were collected at 1, 2, 3, 5, and 10-hour intervals, with simultaneous replenishment of 10 mL fresh 0.5 M H_2SO_4 solution to maintain a constant total electrolyte volume.

The dissolution behavior of metal ions from the catalyst was quantitatively evaluated through Inductively coupled plasma mass spectrometry **(**ICP-MS) analysis of the collected electrolyte samples. The analytical procedure

consisted of the following steps: 1) Calibration curve construction. A series of standard solutions (containing Co, Sb) with concentrations spanning the expected sample range was prepared. Each standard solution was measured five times to establish the relationship between elemental concentration (x-axis) and corresponding emission intensity (y-axis). 2) Sample analysis. All electrolyte samples were analyzed in quintuplicate under identical instrumental conditions. The measured emission intensities for Co and Sb were correlated with the calibration curves to determine their respective concentrations.

Electrochemical characterizations

All electrochemical experiments were performed at 30℃ using a CHI 760E electrochemical workstation with a standard three-electrode system. The electrocatalyst-decorated RDE with glassy carbon was used as the working electrode. The diameter of glassy carbon was 5 mm and the disk area was 0.19625 cm^2. Prior to testing, the glassy carbon electrode was polished for 2 min using 0.5 μm alumina polishing slurry to remove surface oxygen-containing species. Subsequently, it was ultrasonically cleaned sequentially with ultrapure water and ethanol (three cycles each), yielding a pristine electrode surface. The carbon rod and Hg/Hg_2Cl_2 electrode (saturated KCl solution) were applied as the counter electrode and reference electrode, respectively.

Calibration of the saturated calomel electrode (SCE) against the reversible hydrogen electrode (RHE) was performed as follows: H_2 gas was bubbled through the electrolyte for ≥30 min to achieve hydrogen saturation. A platinum foil working electrode was immersed in the H_2-saturated electrolyte, and its open-circuit potential (OCP) was monitored until stabilization (Figure S59). The recorded potential difference between SCE and the Pt electrode (now functioning as RHE) was taken as the offset potential. All subsequent potentials were converted to the reversible hydrogen electrode (RHE) scale using the following equation:

$$E\ (V\ vs.\ RHE) = E\ (V\ vs.\ Hg/Hg_2Cl_2) + 0.248\ (V).$$

The electrocatalyst was prepared with a recipe of 3 mg pre-synthesized catalyst and 0.6 mL solvent of isopropyl alcohol containing 0.1 wt. % Nafion®, which was sonicated for 0.5 hours to be a homogeneous catalyst ink. Then 24 μL catalyst ink was dripped on the surface of the glassy carbon with the total loading of 0.12 mg. Linear sweep voltammetry (LSV) was performed in an Ar-saturated 0.5 M H_2SO_4 electrolyte at a scan rate of 5 mV s^{-1}. The potential was first swept anodically from 1.0 to 1.6 V vs. RHE, followed by a cathodic sweep back to 1.0 V vs. RHE. Following linear sweep voltammetry (LSV), electrochemical impedance spectroscopy (EIS) was conducted under identical experimental conditions to determine the uncompensated solution resistance (R_u) for *iR* compensation. EIS spectra were acquired at open-circuit potential (OCP) over a frequency range of 0.01 Hz to 215.8 kHz with a 5

mV RMS sinusoidal perturbation. The derived (R_u) value (extracted from the real impedance component at 1.0 kHz) was subsequently applied for potential correction using:

$$E_{iR} = E - iR_u$$

where (E) denotes the measured potential and (i) represents the instantaneous current.

For *in situ* EIS studies, the applied potential was systematically varied from 1.50 to 1.70 V vs. RHE in sequential increments. At each constant potential, EIS measurements were conducted with identical frequency parameters and amplitude. Cyclic voltammetry (CV) measurements were performed in the non-Faradaic potential region (1.25-1.35 V vs. RHE) at scan rates of 10, 20, 30, 40, and 50 mV s^{-1}. Each cycle is initiated with an anodic sweep from 1.25 to 1.35 V, immediately followed by a cathodic sweep returning to 1.25 V. The electrochemically active surface areas (ECSA) were estimated from the electrochemical double-layer capacitance (C_{dl}) of the catalytic surface. The C_{dl} was determined by plotting the $\Delta j/2$ ($\Delta j = j_1 - j_2$, where j_1 is the anodic current and j_2 is the cathodic current at the middle voltage) against the scan rate, where the slope is equal to C_{dl}. The electrochemical surface area (ECSA) values were obtained from the electrochemical double-layer capacitance of the catalytic surface, according to: ECSA = C_{dl} /C_s, where C_s is the specific capacitance of the sample (set as 0.035 mF cm^{-2}).

Catalyst stability was evaluated via chronopotentiometry in a standard three-electrode configuration. First, 3 mg of catalyst was ultrasonically dispersed for 30 min in an isopropanol solution containing 0.1 wt% Nafion® to form a homogeneous catalyst ink. The ink was then uniformly drop-casted onto a conductive carbon cloth substrate (1 × 1 cm^2 geometric area) and dried at 60°C for 1 h. The prepared electrode was mounted onto a carbon rod current collector. Chronopotentiometric measurements were performed in 0.5 M H_2SO_4 electrolyte under a constant current density of 10 mA cm^{-2} at 30°C.

Effect of TMA^+ on OER Kinetics. Linear sweep voltammetry (LSV) was first performed in 0.5 M H_2SO_4 electrolyte. Subsequently, the electrolyte was replaced with 0.5 M H_2SO_4 containing 0.01 M tetramethylammonium ions (TMA^+), and LSV measurements were repeated under identical conditions (scan rate: 5 mV s^{-1}, Ar-saturated, 30°C).

Kinetic isotope effects (KIEs) were determined from oxygen evolution reaction (OER) polarization curves measured in protic (H_2SO_4/H_2O) and deuterated (D_2SO_4/D_2O) electrolytes. After baseline LSV in H_2O-based electrolyte, the electrochemical cell was disassembled and all components (including working electrode) were soaked in D_2O for 30 min. Following reassembly, triple rinsing with D_2O preceded filling with deuterated electrolyte. LSVs were recorded under identical conditions (scan rate: 5 mV s^{-1}, 1.0-1.6 V vs. RHE, Ar-saturated, 30°C).

Calibration of the saturated calomel electrode (SCE) against reversible deuterium electrode (RDE) was

performed as follows: D_2 gas was bubbled through the electrolyte for ≥30 min to achieve deuterium saturation. A platinum foil working electrode was immersed in the D_2-saturated electrolyte, and its open-circuit potential (OCP) was monitored until stabilization (Figure S60). The recorded potential difference between SCE and the Pt electrode (now functioning as RHE) was taken as the offset potential. The potential on a reversible deuterium electrode (RDE) was derived using the formula:

$$E\ (V\ vs.\ RDE) = E\ (V\ vs.\ Hg/Hg_2Cl_2) + 0.286\ (V)$$

The KIE was then obtained by:

$$KIE = \left|\frac{jH2O}{jD2O}\right|$$

where j_{H2O} and j_{D2O} represent the respective current densities in the protonic and deuteric solutions at the same overpotential.

PEMWE measurements

(1) Fabrication of Membrane Electrode Assembly (MEA) for PEM Water Electrolysis

Anode catalysts ($Sb_{0.3}Co_{2.7}O_4$ or Co_3O_4, 4 mg) and cathode catalysts (20 wt% Pt/C, 2 mg) were separately dispersed in 8 mL and 4 mL of isopropanol solutions containing 0.1 wt% Nafion®, respectively. Homogeneous suspensions were obtained through ultrasonication in an ice-water bath for 2 h. The resulting anode and cathode catalyst inks were uniformly sprayed onto opposing sides of a Nafion 115 proton exchange membrane (1×1 cm^2 active area, Figure S39) using an airbrush system. During spraying, the membrane was secured on a temperature-controlled vacuum platform (60°C) to accelerate solvent evaporation. This process yielded catalyst loadings of 2 mg cm^{-2} (anode) and 1 mg cm^{-2} (cathode). The catalyst-coated membrane was subsequently hot-pressed at 130°C under 3 MPa pressure for 3 minutes. The processed membrane was then assembled with a platinum-coated titanium felt anode (0.15 mg cm^{-2} Pt loading) and carbon paper cathode (Sigracet® 29BC) to form the complete MEA. This assembly was integrated into a proton exchange membrane water electrolysis (PEMWE) test cell, with all components tightened to a controlled torque of 5 N·m using calibrated torque drivers (Figure S36).

(2) The assembly of the PEMWE

The PEMWE cell was integrated with a temperature-controlled water circulation system. Deionized water preheated to 80 °C was circulated through the anode chamber at a constant flow rate of 35 mL min^{-1} using a peristaltic pump. The cathode outlet was connected to a gas-liquid separator for hydrogen collection. To maintain

isothermal conditions, an integrated heating jacket with PID control was employed, ensuring uniform cell temperature at 80 ± 0.1 °C. Real-time temperature stabilization was achieved through a feedback control system. As illustrated in Figure S35, high-precision temperature sensors were embedded within the anode to monitor interfacial temperatures adjacent to the membrane electrode assembly (MEA). The sensor signals were transmitted to a temperature controller, which dynamically adjusted the heating jacket power to maintain the MEA operating temperature at 80 ± 0.1 °C throughout all experiments.

(3) Testing details of the PEMWE

Electrochemical characterization was performed using a Newell testing system. Polarization curves were obtained by applying a step-current protocol with 0.2 A increments. Current density (mA cm^{-2}) was plotted against cell potential (V) to systematically evaluate the electrochemical performance under controlled temperature. The polarization curves with error bars were obtained by testing three sets of membrane electrodes prepared with the same catalyst.

(4) Parameter calculation method

Energy efficiency calculation: The energy efficiency of PEMWE is calculated based on the following equation:

$$Energy\ efficiency\ = 1.481\ V/U_{cell}$$

where 1.481 V represents the higher heating value of H_2, U_{cell} is the cell voltage (V).

Voltage degradation rate: The voltage degradation rate was determined by durability tests at a constant current density. The cell voltage was recorded as a function of time, and the degradation rate (μV h^{-1}) was calculated from the slope of the linear fit of the voltage-time curve after the initial break-in period, following previously established methodologies.

DFT calculations

All the theoretical calculations were conducted by using CASTEP code of the Materials Studio package of Accelrys Inc with generalized gradient approximation method (GGA) and the Perdew-Burke-Ernzerh (PBE) functional to describe the exchange and correlation interactions [11]. The interaction between valence electrons and

ionic cores was described by Ultrasoft pseudopotential [12]. The cutoff energy was set as 400 eV and the self-consistent field (SCF) tolerance was 1×10^{-6} eV. We choose (311) surface as the model of Sb doped Co_3O_4 and Co_3O_4 for calculation. The smearing method of Methfessel-Paxton (MP) and smearing widths of 0.1 eV were applied to optimize the geometric [13]. The Brillouin zone was sampled using the Monkhorst Pack method, and the number of k points was set according to the model, of which 3×3×1 was set for all the geometric optimization. The thickness of vacuum layer along the z-direction is set as 15 Å to separate the upper and lower surfaces. For all calculations, the atoms in the bottom layer were fixed in the equilibrium positions, while the rest of the atoms were fully relaxed.

Accordingly, the Gibbs free energy changes for the water oxidation steps using AEM mechanism were calculated using the following Equations:

$$H_2O + M^* \rightarrow M - OH + e^- + H^+ \quad (\Delta G_1)$$

$$M - OH \rightarrow M - O + H^+ + e^- \quad (\Delta G_2)$$

$$H_2O + M - O \rightarrow M - OOH + H^+ + e^- \quad (\Delta G_3)$$

$$M - OOH \rightarrow M + O_2 + H^+ + e^- \quad (\Delta G_4)$$

The Gibbs free energy changes for the water oxidation steps using OPM mechanism were calculated using the following Equations:

$$H_2O + M\,{*}\text{-}\,M^* \rightarrow M\,{*}\text{-}\,M - OH\,{*} + H^+ + e^-$$

$$H_2O + M\,{*}\text{-}\,M - OH^* \rightarrow O\,{*}\text{-}\,M\,{*}\text{-}\,M - OH\,{*} + 2H^+ + 2e^-$$

$$O\,{*}\text{-}\,M\,{*}\text{-}\,M - OH^* \rightarrow M - OO - M + H^+ + e^-$$

$$M - OO - M \rightarrow M\,{*}\text{-}\,M\,{*} + O_2$$

where * denotes adsorption active site on the substrate.

The Gibbs free energy of the adsorbed intermediate can be calculated as ΔG = ΔE + ΔZPE - TΔS, where ΔE is the DFT-computed adsorption energy, and ΔZPE and TΔS are the zero-point energy and entropy corrections, respectively.

It should be noted that we investigated the electrochemical processes by employing the established computational hydrogen electrode (CHE) model. The theoretical basis for the validity of the CHE model is that electrochemical reactions happened in the solution normally possess small kinetic barriers, which are surmountable at room temperature. The reaction kinetics thus be dictated by merely the free energy difference of each step. Therefore, the step with the most positive free energy difference is the rate-determining step. As a result, the theoretical overpotential η is defined in equation:

$$\eta_{theory} = \frac{\max\{\Delta G_1, \Delta G_2, \Delta G_3, \Delta G_4\}}{e} - 1.23V$$

Ab initio molecular dynamics (AIMD) theoretical simulation

All the periodic models with explicit solvent in this work were pre-equilibrated in Vienna Ab-initio Simulation Package (VASP) code. During geometry optimization, the cut-off energy was set as 500 eV for structures, respectively. The Brillouin zone was sampled by a Monkhorst-Pack (MP) k-point grid of 1×1×1 for geometry optimizations. Then it was simulated with ab initio molecular dynamics (AIMD) for 10 ps in the canonical (NVT) ensemble, maintaining a constant temperature of 300 K by Nosé-Hoover thermostat method, where the timestep was set to 1 fs.

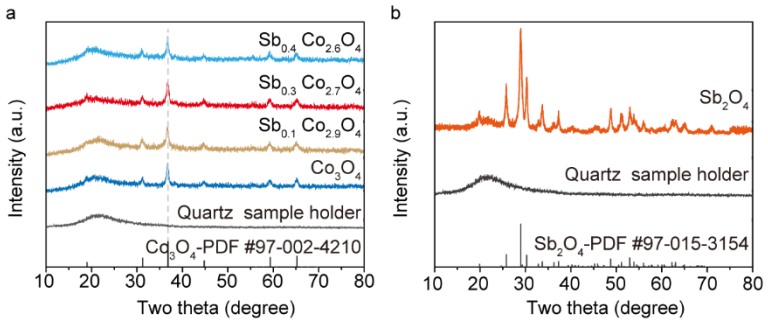

Figure S1. XRD patterns of (a) Co_3O_4, $Sb_{0.4}Co_{2.6}O_4$, $Sb_{0.3}Co_{2.7}O_4$, and $Sb_{0.1}Co_{2.9}O_4$ and (b) Sb_2O_4; the broad peak at around 20 degrees is attributed to the quartz sample holder.

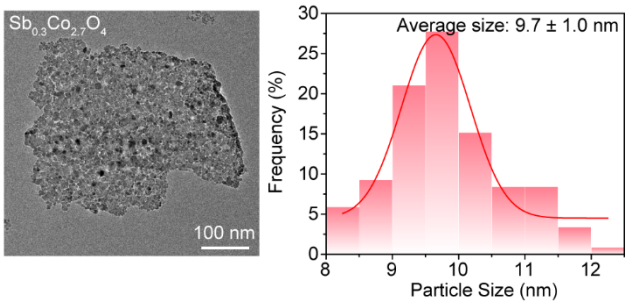

Figure S2. TEM image of $Sb_{0.3}Co_{2.7}O_4$ and the corresponding particle size distribution.

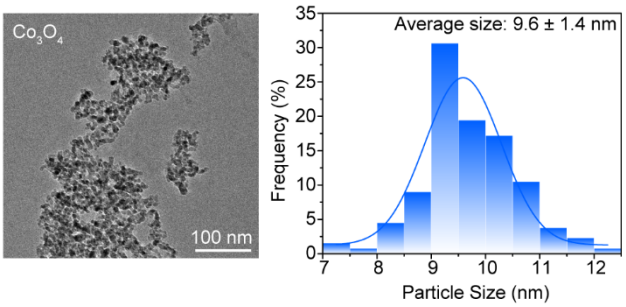

Figure S3. TEM image of Co_3O_4 and the corresponding particle size distribution.

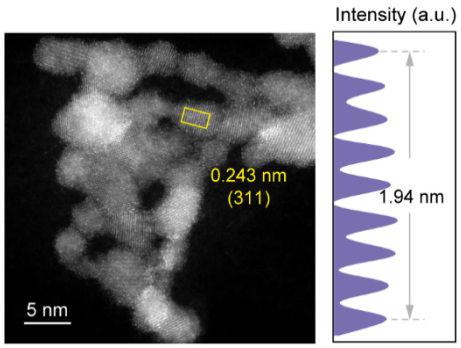

Figure S4. HRTEM images of $Sb_{0.3}Co_{2.7}O_4$.

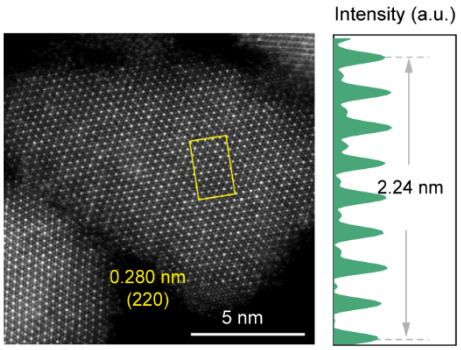

Figure S5. HRTEM images of $Sb_{0.3}Co_{2.7}O_4$.

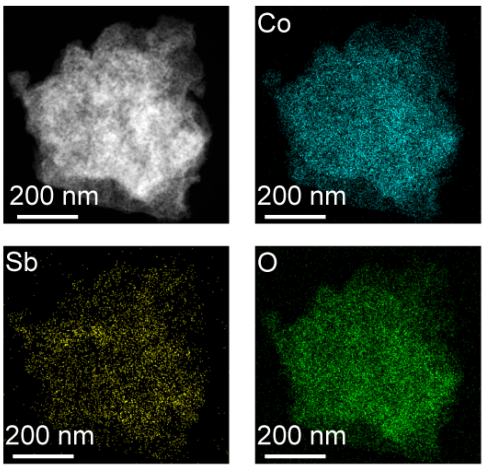

Figure S6. Elemental mapping of $Sb_{0.3}Co_{2.7}O_4$ at a 200 nm scale.

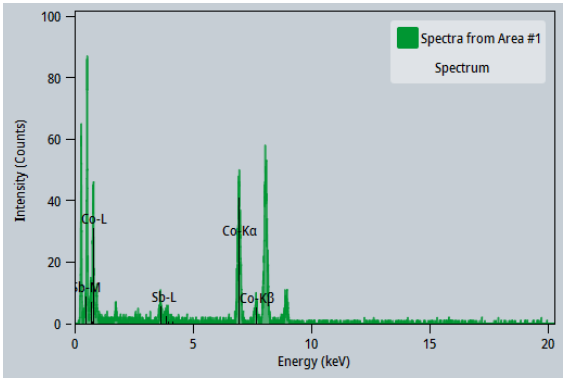

Figure S7. The EDS spectra of $Sb_{0.3}Co_{2.7}O_4$ at a 200 nm scale.

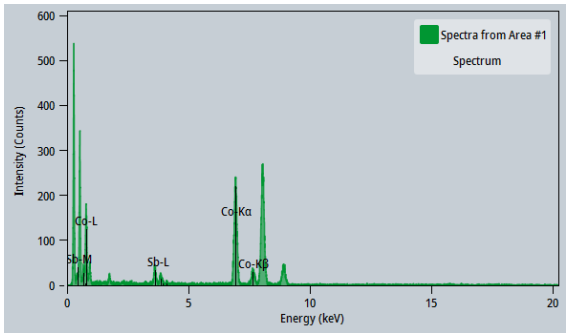

Figure S8. The EDS spectra of $Sb_{0.3}Co_{2.7}O_4$ at a 100 nm scale.

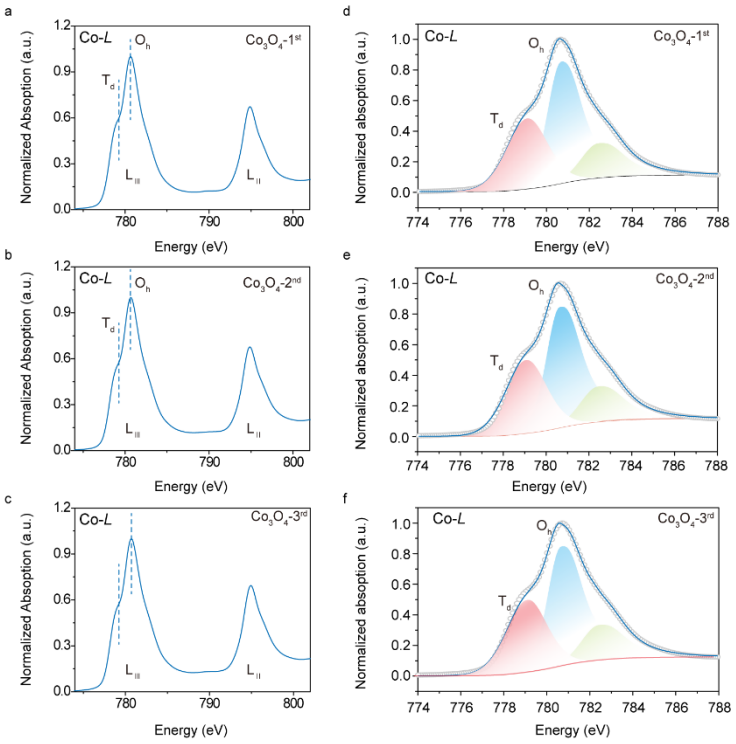

Figure S9. Soft X-ray absorption spectroscopy (XAS) at the Co *L*-edge of the Co_3O_4 samples (with three experimental repeats).

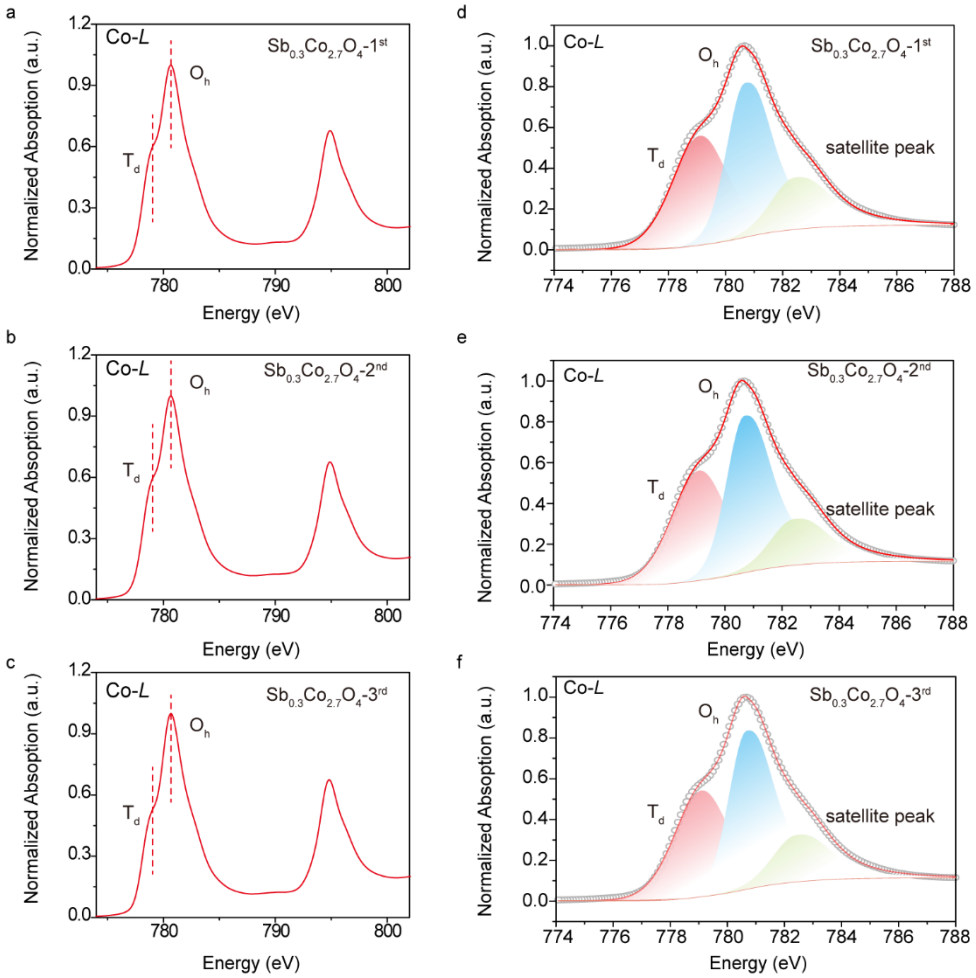

Figure S10. Soft X-ray absorption spectroscopy (XAS) at the Co *L*-edge of the $Sb_{0.3}Co_{2.7}O_4$ samples (with three experimental repeats).

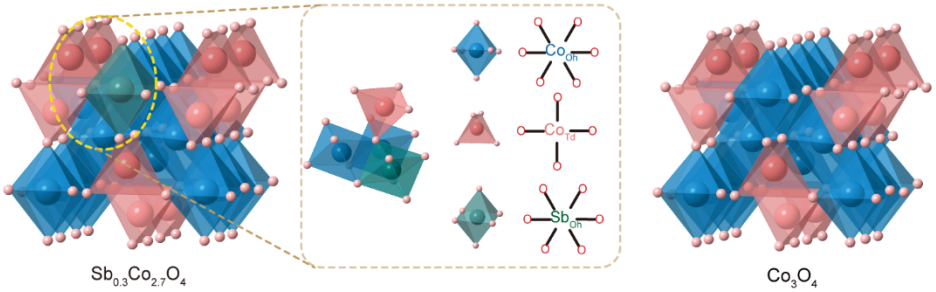

Figure S11. Crystal structures of $Sb_{0.3}Co_{2.7}O_4$ and Co_3O_4.

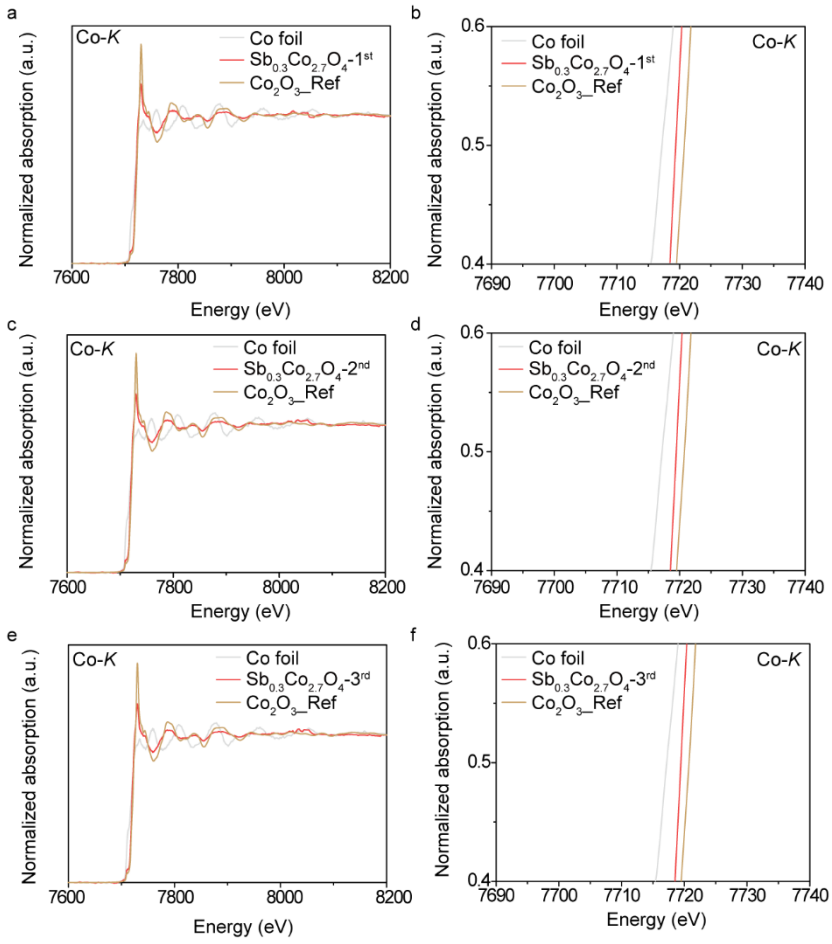

Figure S12. XANES spectra at Co *K*-edge of Co foil, $Sb_{0.3}Co_{2.7}O_4$, and Co_2O_3_Ref samples (with three experimental repeats).

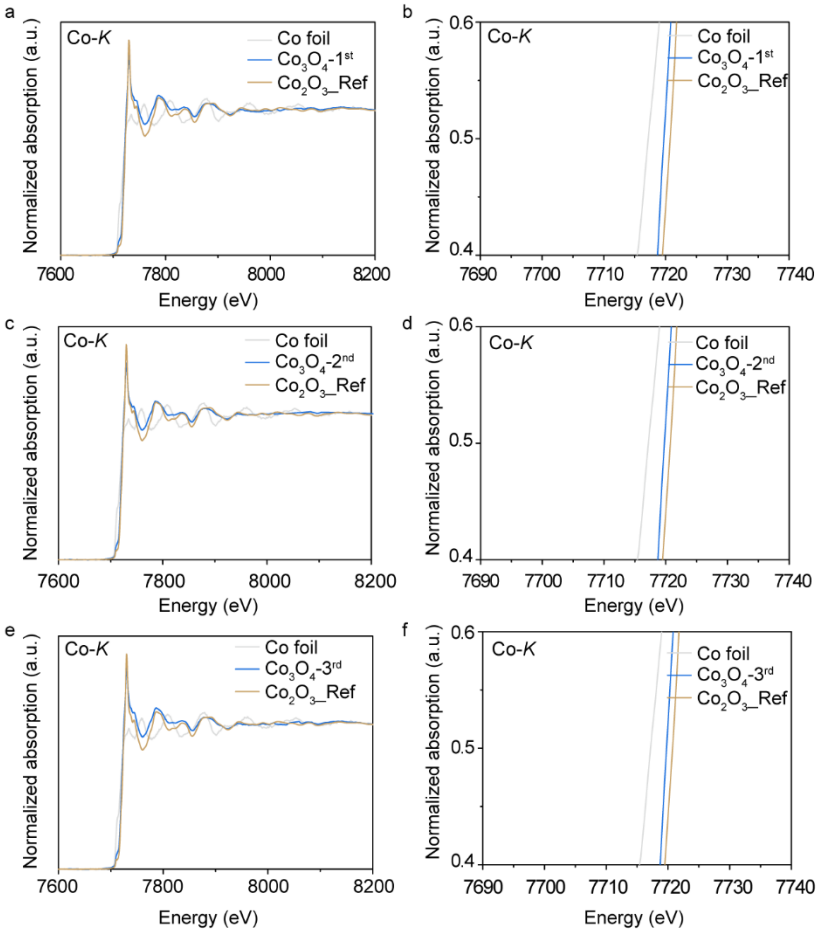

Figure S13. XANES spectra at Co *K*-edge of Co foil, Co_3O_4, and Co_2O_3_Ref samples (with three experimental repeats).

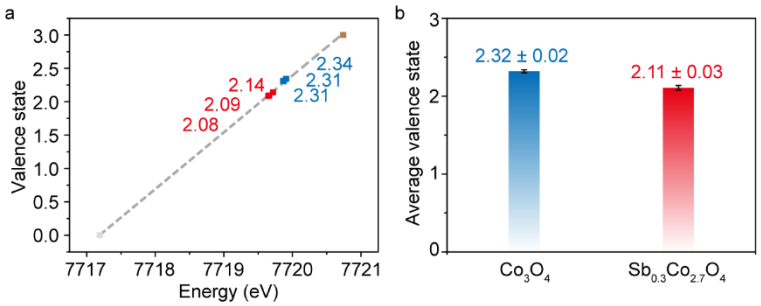

Figure S14. The oxidation state of Co species in $Sb_{0.3}Co_{2.7}O_4$ and Co_3O_4 obtained from Co *K*-edge XANES (with three experimental repeats) and the comparison of the average Co oxidation states obtained from Co *K*-edge XANES.

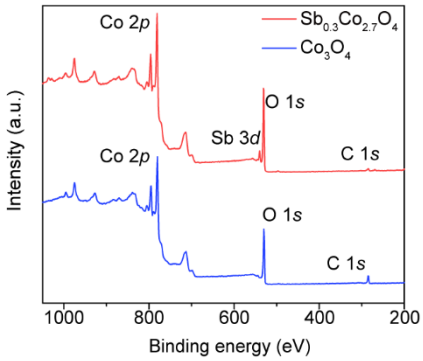

Figure S15. XPS survey of $Sb_{0.3}Co_{2.7}O_4$ and Co_3O_4.

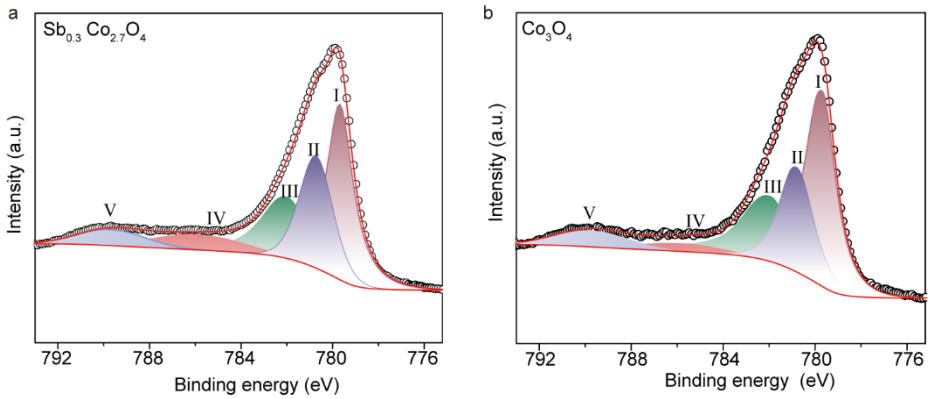

Figure S16. High-resolution XPS spectrum of $Sb_{0.3}Co_{2.7}O_4$ and Co_3O_4.

As shown in Figure S16 and Table S4, the Co $2p_{3/2}$ XPS spectrum of $Sb_{0.3}Co_{2.7}O_4$ and Co_3O_4 was deconvoluted into components corresponding to Co^{2+} and Co^{3+} species, along with their characteristic satellite peaks. The peaks at ~779.60 eV and ~781.96 eV are attributed to Co^{2+}, while the component at ~780.80 eV is assigned to Co^{3+}. The satellite features at ~785.78 eV and ~789.71 eV correspond to the Co^{2+} satellite and the Co^{3+} satellite, respectively [1-2]. Quantitative analysis shows that the introduction of Sb leads to a decrease in the Co^{3+} proportion from 48.1% in pristine Co_3O_4 to 44.7% in $Sb_{0.3}Co_{2.7}O_4$. This reduction in the average oxidation state of cobalt is consistent with the trend observed in our XAS analysis, further supporting the effective incorporation of Sb and its influence on the electronic structure of Co_3O_4.

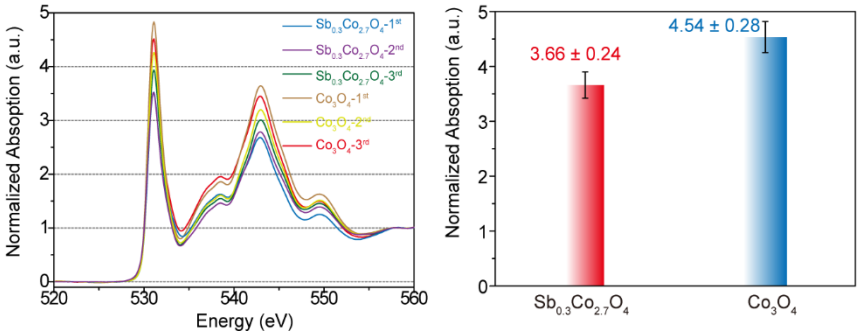

Figure S17. Normalized O *K*-edge XAS spectra of $Sb_{0.3}Co_{2.7}O_4$ and Co_3O_4 samples (with three experimental repeats).

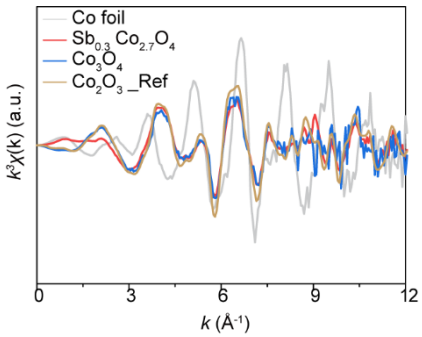

Figure S18. k^3-weighted χ(k) spectra of Co foil, Co_3O_4, $Sb_{0.3}Co_{2.7}O_4$ and Co_2O_3_Ref.

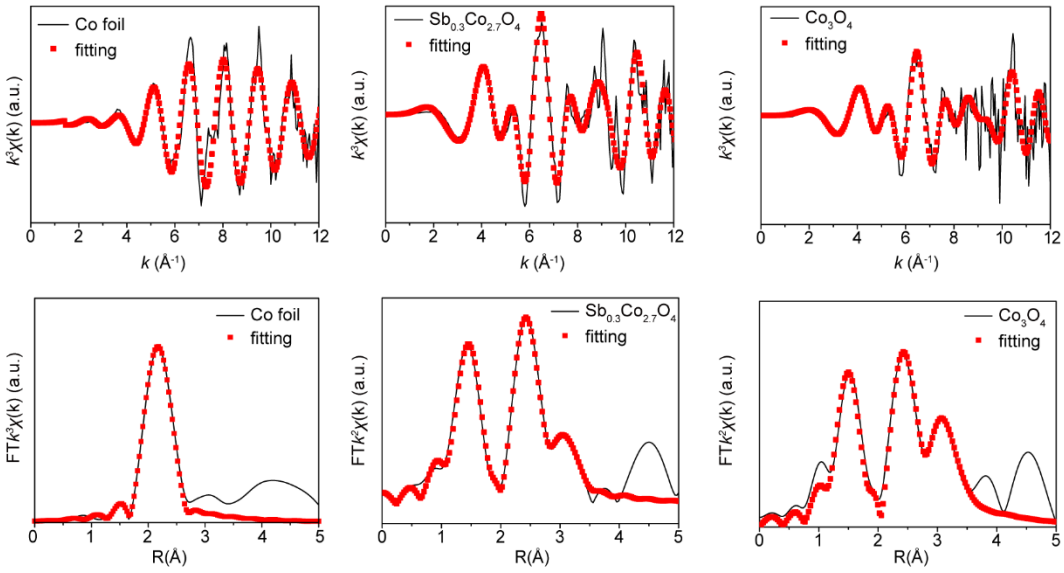

Figure S19. EXAFS fitting results at the Co *K*-edge of Co foil, $Sb_{0.3}Co_{2.7}O_4$ and Co_3O_4.

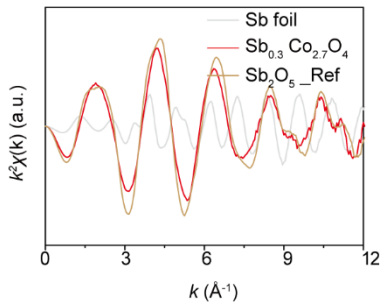

Figure S20. k^2-weighted χ(k) spectra of Sb foil, $Sb_{0.3}Co_{2.7}O_4$, and Sb_2O_5_Ref.

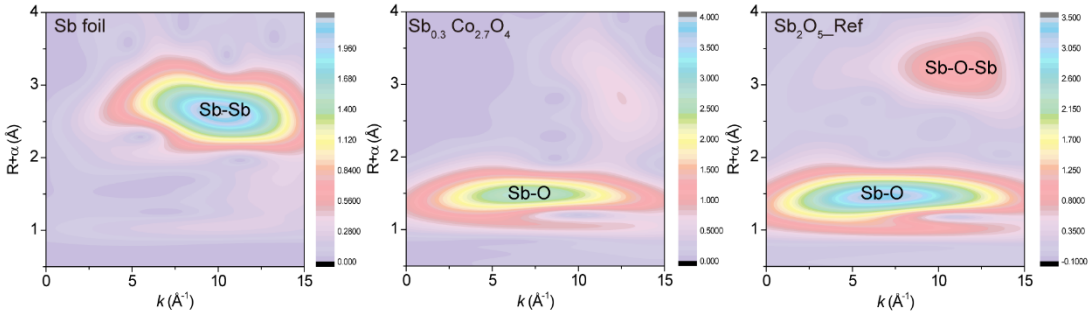

Figure S21. Wavelet transform of Co K-edge EXAFS data of Sb foil, $Sb_{0.3}Co_{2.7}O_4$, and Sb_2O_5_Ref.

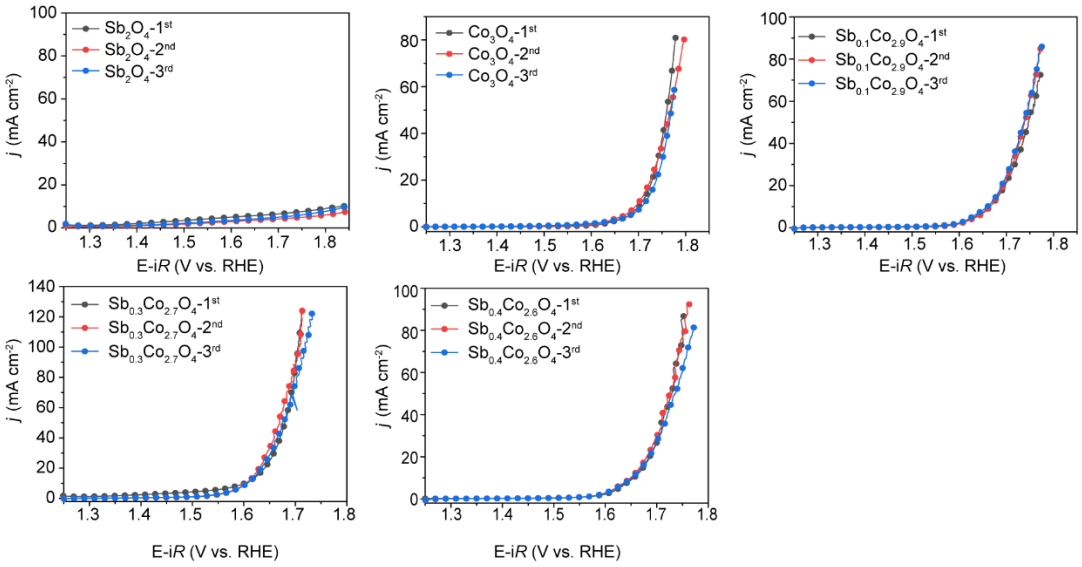

Figure S22. OER polarization curves of various catalysts (data obtained from three different samples under the same testing conditions).

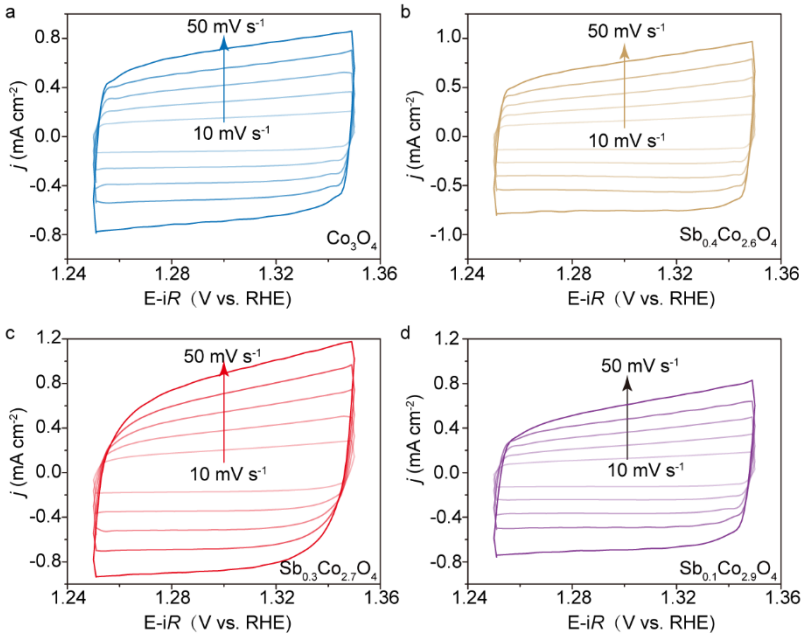

Figure S23. CV curves with different sweep speeds of (a) Co_3O_4, (b) $Sb_{0.4}Co_{2.6}O_4$, (c) $Sb_{0.3}Co_{2.7}O_4$, and (d) $Sb_{0.1}Co_{2.9}O_4$.

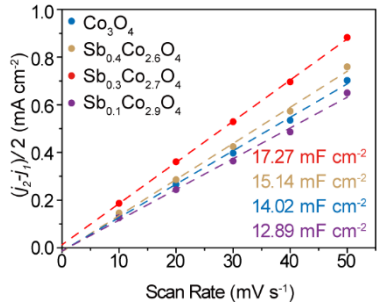

Figure S24. C_{dl} plots of Co_3O_4, $Sb_{0.4}Co_{2.6}O_4$, $Sb_{0.3}Co_{2.7}O_4$, and $Sb_{0.1}Co_{2.9}O_4$ obtained from CV curves.

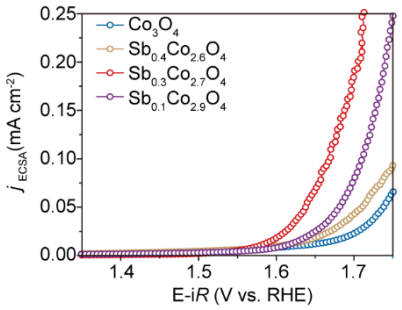

Figure S25. LSV curves of Co_3O_4, $Sb_{0.4}Co_{2.6}O_4$, $Sb_{0.3}Co_{2.7}O_4$, and $Sb_{0.1}Co_{2.9}O_4$ normalized by ECSA.

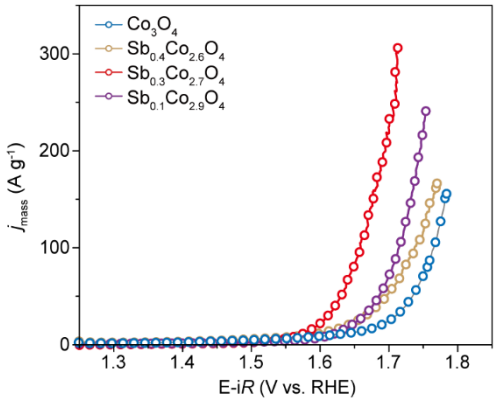

Figure S26. LSV curves of Co_3O_4, $Sb_{0.4}Co_{2.6}O_4$, $Sb_{0.3}Co_{2.7}O_4$ and $Sb_{0.1}Co_{2.9}O_4$ normalized by mass.

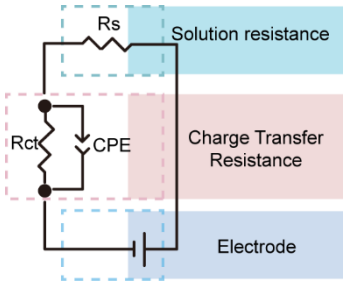

Figure S27. Equivalent circuit-fitting EIS for $Sb_{0.3}Co_{2.7}O_4$ and Co_3O_4.

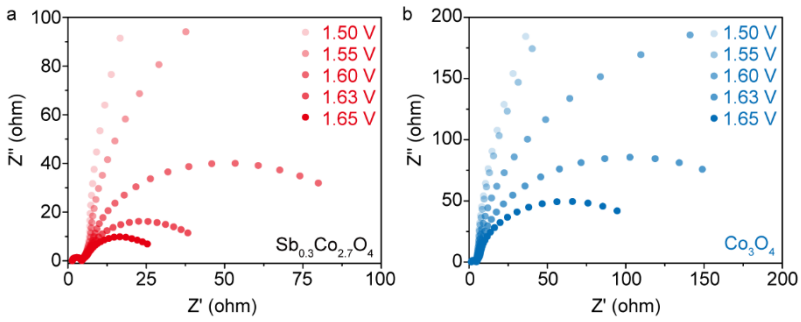

Figure S28. Nyquist plots for (a) $Sb_{0.3}Co_{2.7}O_4$ and (b) Co_3O_4 catalysts at different applied potentials versus RHE in 0.5 M H_2SO_4.

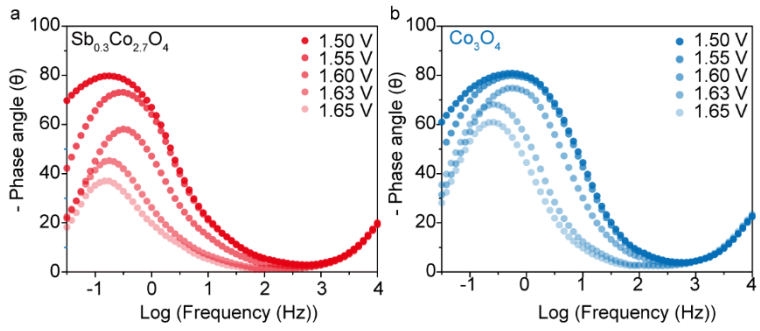

Figure S29. Bode phase plots of $Sb_{0.3}Co_{2.7}O_4$ (a), Co_3O_4 (b), at different potentials versus RHE in 0.5 M H_2SO_4.

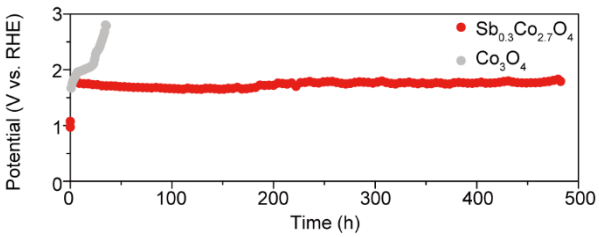

Figure S30. Chronopotentiometry curves of $Sb_{0.3}Co_{2.7}O_4$ and Co_3O_4 at a current density of 10 mA cm^{-2}.

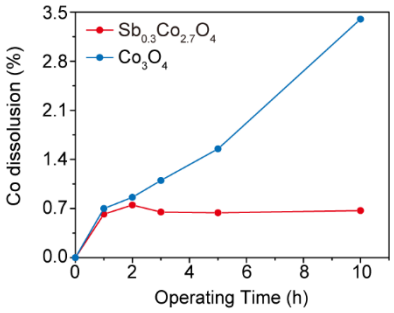

Figure S31. Co dissolved mass fraction of $Sb_{0.3}Co_{2.7}O_4$ and Co_3O_4 after operating times of 1, 2, 3, 5, and 10 h under 0.5 M H_2SO_4 electrolyte.

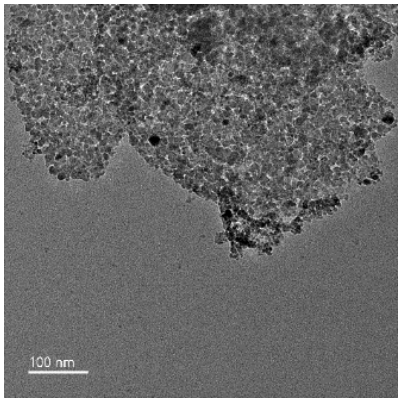

Figure S32. TEM image of $Sb_{0.3}Co_{2.7}O_4$ after the stability test.

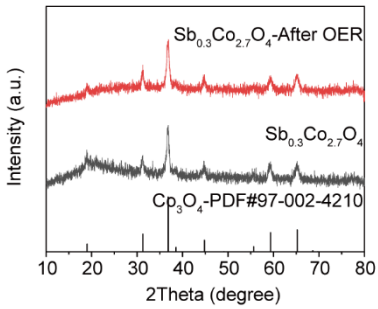

Figure S33. XRD patterns of $Sb_{0.3}Co_{2.7}O_4$ before and after the stability test.

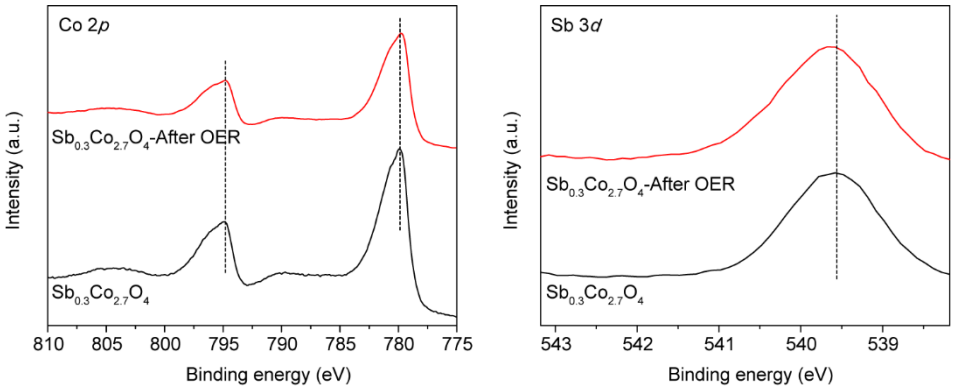

Figure S34. High-resolution XPS spectra of $Sb_{0.3}Co_{2.7}O_4$ before and after the stability test.

Figure S35. Temperature monitoring and real-time control system.

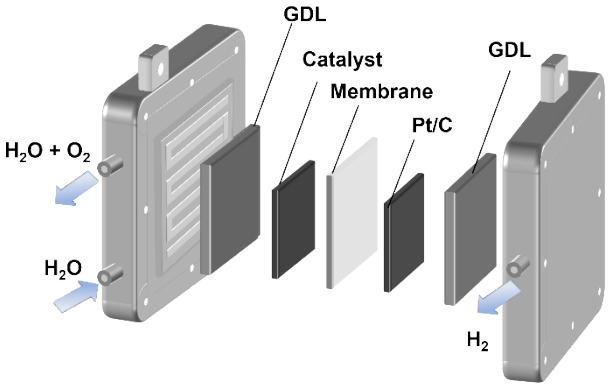

Figure S36. The configuration of the PEMWE electrodes.

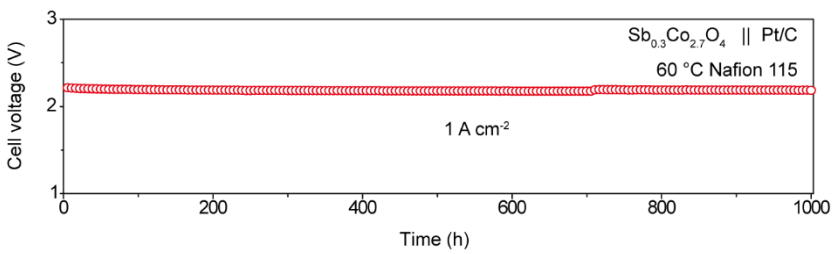

Figure S37. Chronopotentiometry test of $Sb_{0.3}Co_{2.7}O_4$ at 1 A cm^{-2} in a PEMWE electrolyzer.

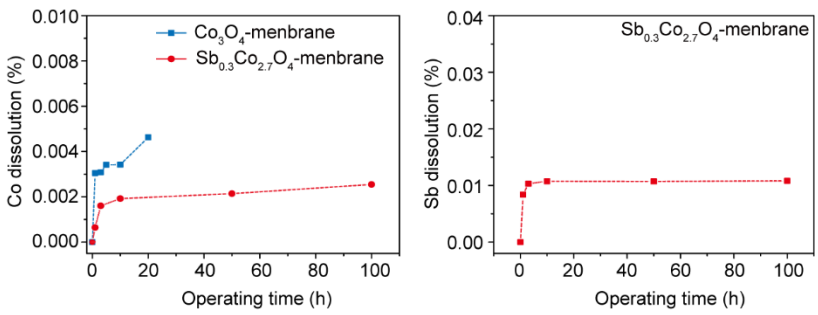

Figure S38. Co-dissolved mass fraction of $Sb_{0.3}Co_{2.7}O_4$-membrane (1, 3, 5, 10, 50, and 100 h) and Co_3O_4-membrane (1, 3, 5, 10, and 20 h) after long-term stability of 1 A cm^{-2} under PEMWE. Sb-dissolved mass fraction of $Sb_{0.3}Co_{2.7}O_4$-membrane (1, 3, 10, 50, and 100 h) after long-term stability of 1A cm^{-2} under PEMWE.

We determined the concentration of dissolved Co and Sb ions in the electrolytes to quantify the dissolution of catalysts by performing ICP-MS analysis at various reaction times by maintaining current density of 1 A cm^{-2} [3-5]. The loading of the anode catalyst was all 2 mg cm^{-2}, and the electrolyte volume was uniformly controlled at 800 ml throughout the PEMWE cycle. As shown in Figure S38, the concentration of dissolved Co ions in Co_3O_4 increases markedly with prolonged reaction time, reaching 0.005% after 30 hours of operation. In contrast, that in $Sb_{0.3}Co_{2.7}O_4$ increases only marginally, with just 0.002% dissolution observed over 100 hours of operation, indicating effective suppression of the dissolution of Co. Correspondingly, the amount of Sb dissolved from the doped sample over the same period of stable operation is 0.010%. Notably, the concentrations of both Co and Sb in the electrolyte remain almost unchanged during the latter half of the stability test, suggesting that no further dissolution of metal ions occurs from $Sb_{0.3}Co_{2.7}O_4$.

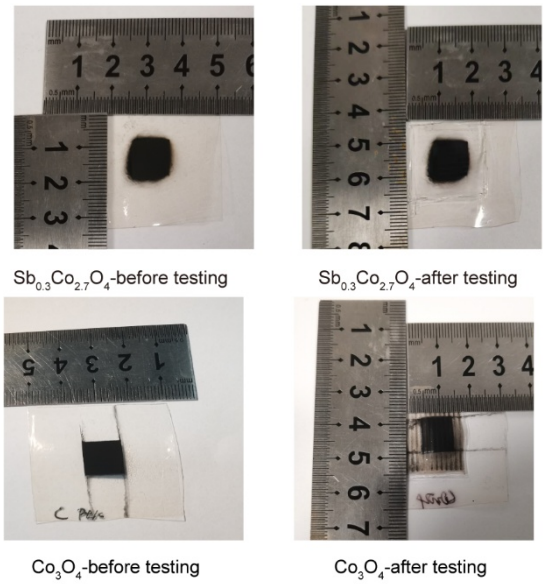

Figure S39. Photos and dimensions of the $Sb_{0.3}Co_{2.7}O_4$-membrane and Co_3O_4-membrane before and after long-term stability testing.

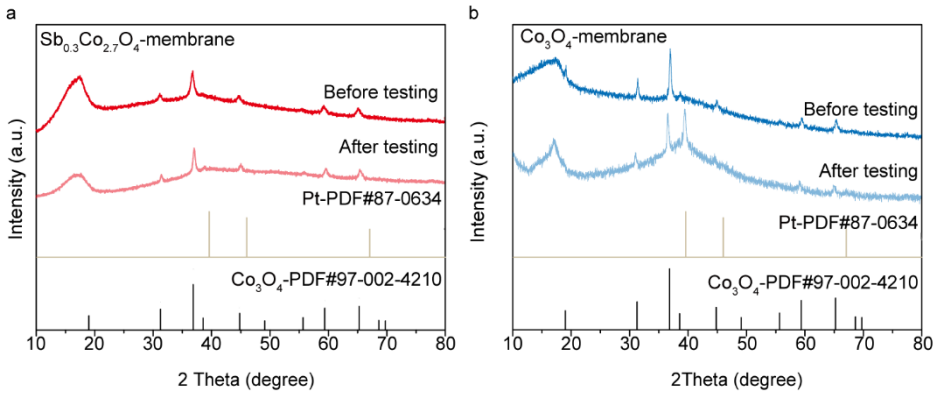

Figure S40. XRD patterns of $Sb_{0.3}Co_{2.7}O_4$-membrane and Co_3O_4-membrane before and after long-term stability testing.

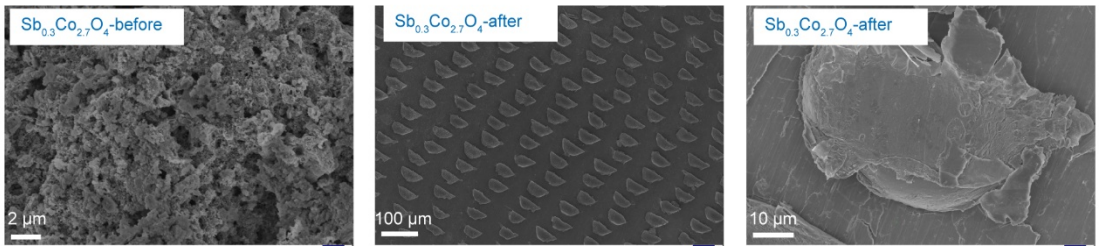

Figure S41. SEM of $Sb_{0.3}Co_{2.7}O_4$-membrane before and after long-term stability testing.

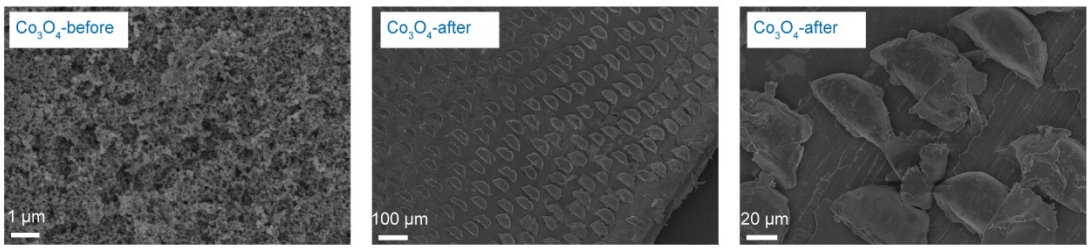

Figure S42. SEM of Co_3O_4-membrane before and after long-term stability testing.

We characterized the MEA of $Sb_{0.3}Co_{2.7}O_4$ after the 1000 h stability test and compared it with the MEA of Co_3O_4 after the 30 h. As shown in Figure S40, both the $Sb_{0.3}Co_{2.7}O_4$-membrane and Co_3O_4-membrane before testing exhibited the characteristic diffraction peaks of Co_3O_4. After long-term stability testing, the $Sb_{0.3}Co_{2.7}O_4$-membrane showed little difference compared to its pre-test state. However, the Co_3O_4-membrane clearly revealed XRD

diffraction peaks corresponding to the cathode Pt catalyst. We hypothesize that this difference arises because the Co_3O_4 anode catalyst dissolved significantly during the stability test, causing the catalyst layer to thin continuously. This thinning allowed detection of the XRD signals from the cathode catalyst, corroborating the relatively poor stability of Co_3O_4 observed during the stability test. In addition, we performed SEM characterization on the MEAs. As shown in Figs S41-S42, the tested catalysts exhibited noticeable indentations, which are primarily attributed to the presence of flow channels in the PEMWE and the applied pressure.

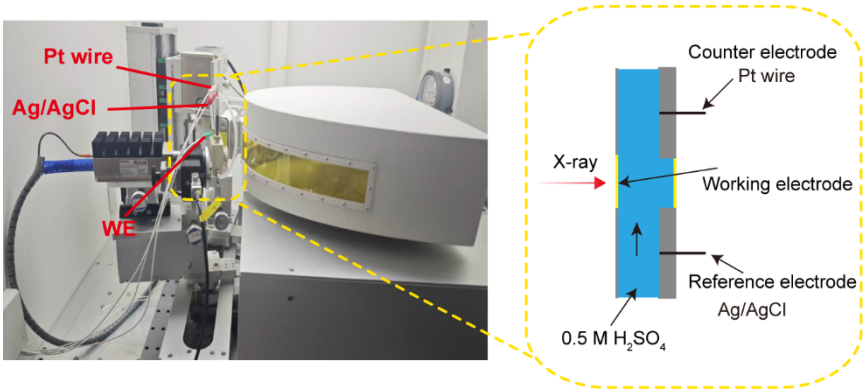

Figure S43. Photos and schematic diagram of X-ray absorption spectroscopy (XAS) device.

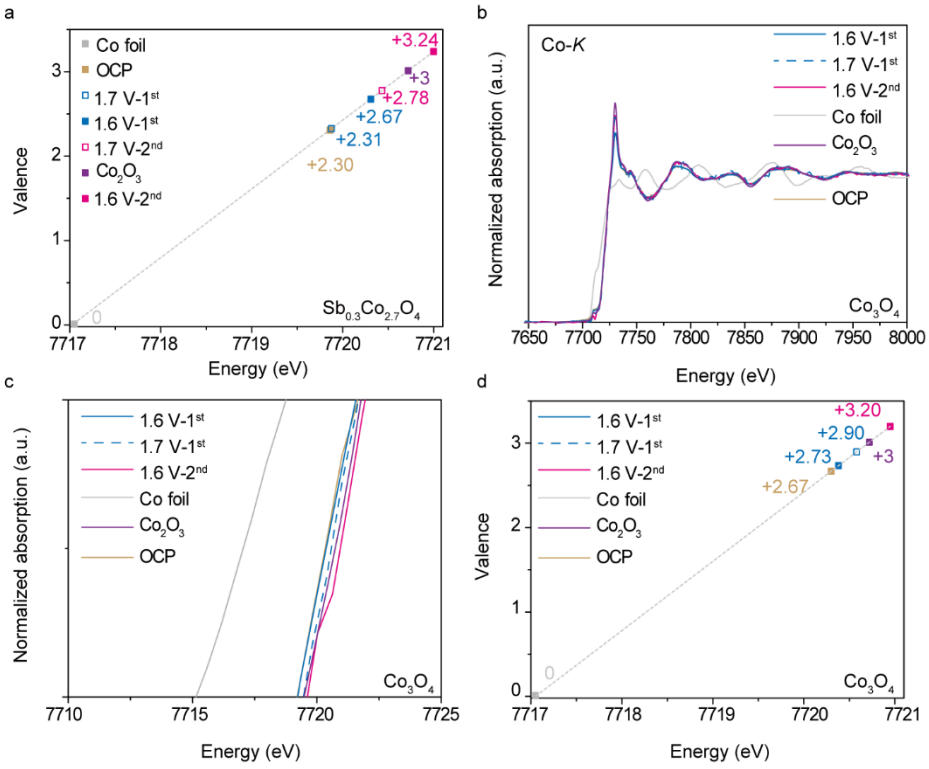

Figure S44. XANES spectra at Co *K*-edge of Co_3O_4 at different potentials and corresponding oxidation of Co in

$Sb_{0.3}Co_{2.7}O_4$ and Co_3O_4 at different potentials.

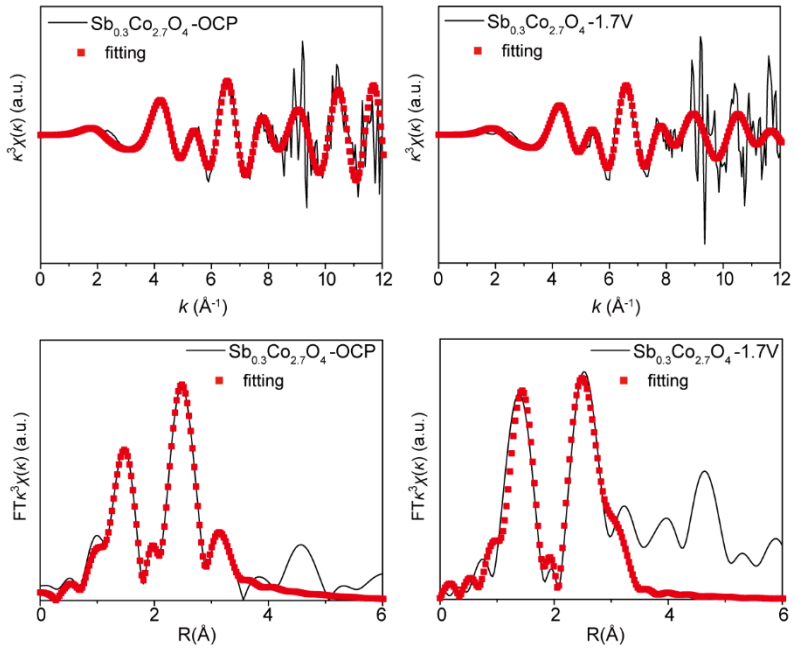

Figure S45. *In-situ* EXAFS fitting results for Co *K*-edge of $Sb_{0.3}Co_{2.7}O_4$-OCP and $Sb_{0.3}Co_{2.7}O_4$-1.7 V.

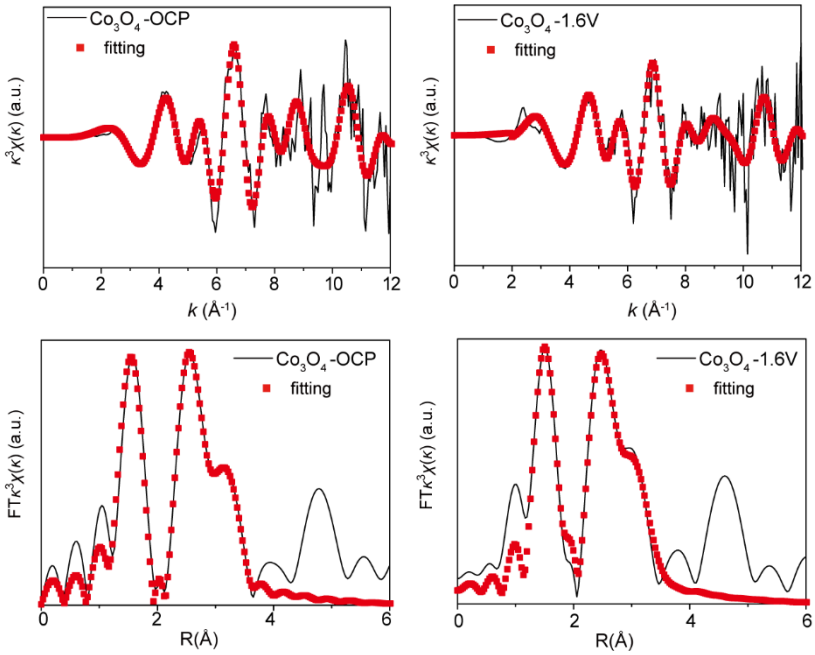

Figure S46. *In-situ* EXAFS fitting results for Co *K*-edge of Co_3O_4-OCP and Co_3O_4-1.6 V.

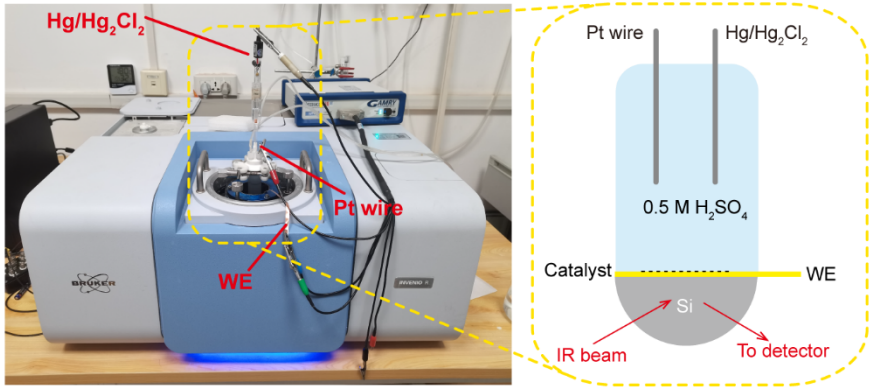

Figure S47. Photos and schematic diagram of *in-situ* attenuated total reflectance-surface-enhanced infrared absorption spectroscopy (ATR-SEIRAS) device.

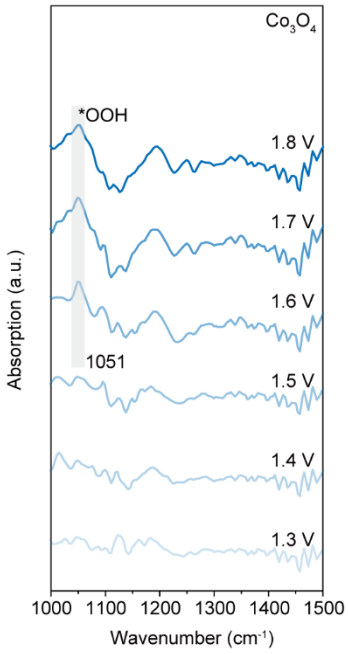

Figure S48. *In-situ* ATR-SEIRAS spectroscopy of Co_3O_4 in 0.5 M H_2SO_4.

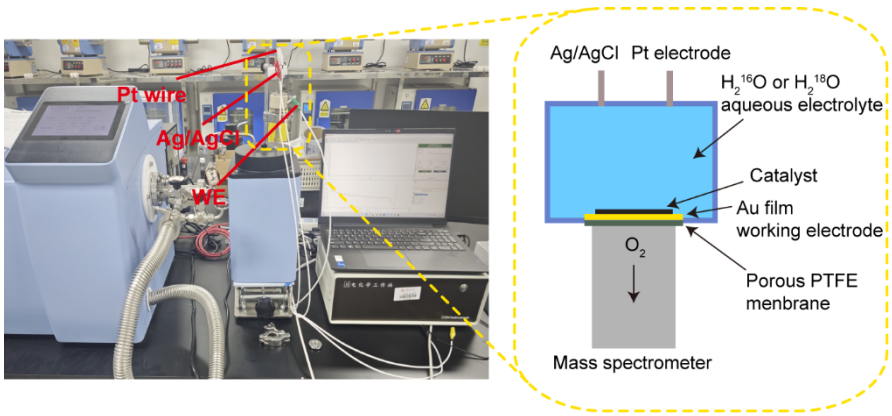

Figure S49. Photos and schematic diagram of *in-situ* ^{18}O isotope labeling differential electrochemical mass spectrometry (DEMS) device.

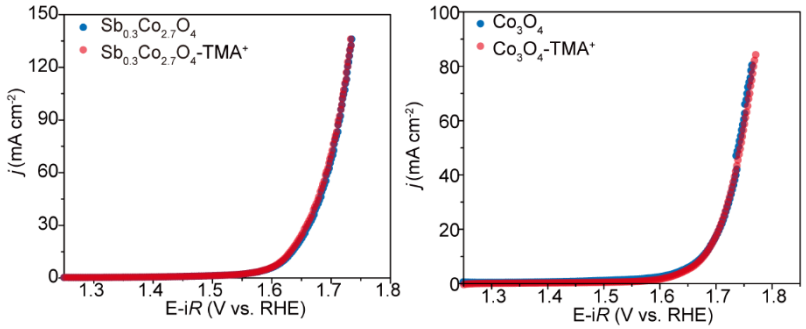

Figure S50. LSV curves of Co_3O_4 in 0.5 M H_2SO_4 electrolyte with or without TMA^+.

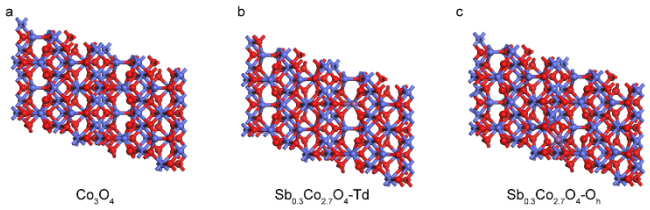

Figure S51. The geometric configurations of Co_3O_4 and $Sb_{0.3}Co_{2.7}O_4$ model.

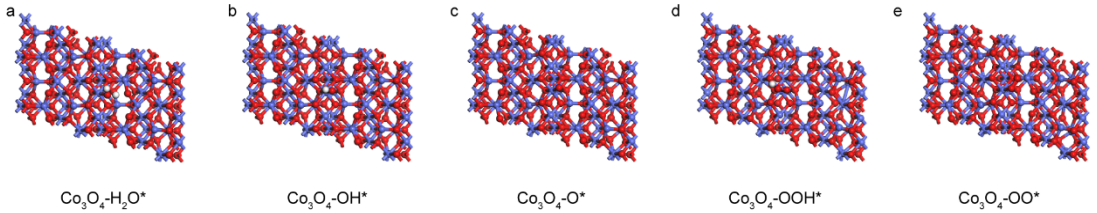

Figure S52. Intermediate adsorption model of Co_3O_4 through AEM.

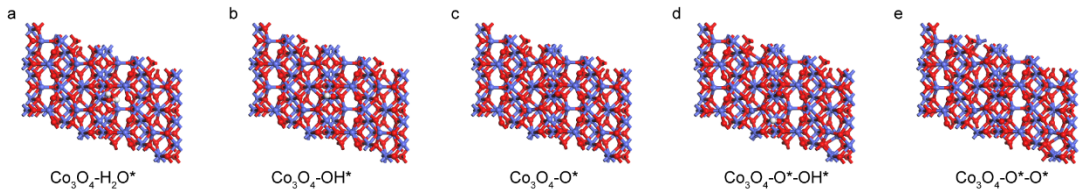

Figure S53. Intermediate adsorption model of Co_3O_4 through OPM.

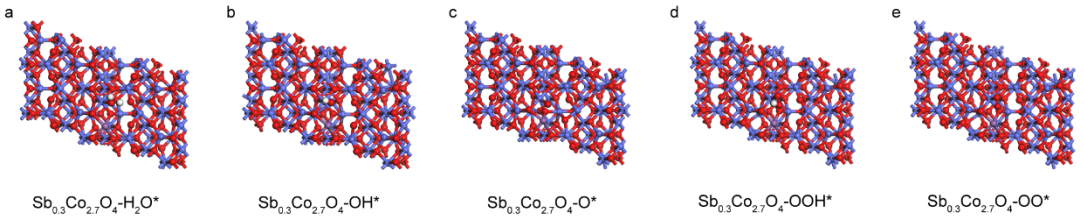

Figure S54. Intermediate adsorption model of $Sb_{0.3}Co_{2.7}O_4$ through AEM.

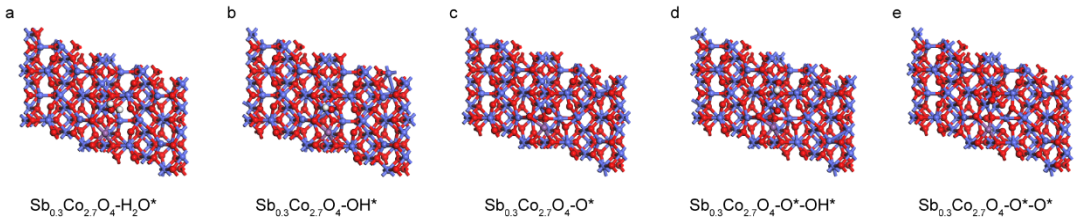

Figure S55. Intermediate adsorption model of $Sb_{0.3}Co_{2.7}O_4$ through OPM via Co-Co dual sites.

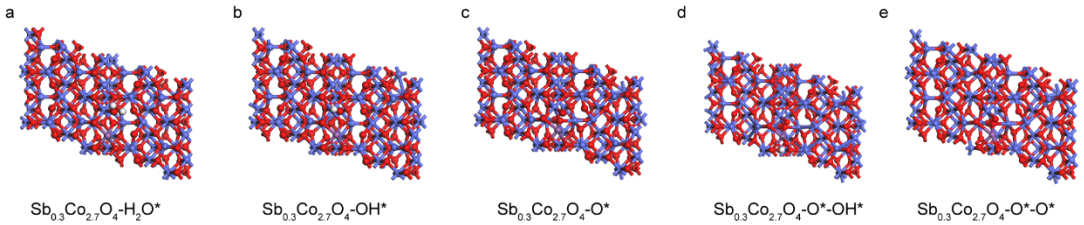

Figure S56. Intermediate adsorption model of $Sb_{0.3}Co_{2.7}O_4$ through OPM via Co-Sb dual sites.

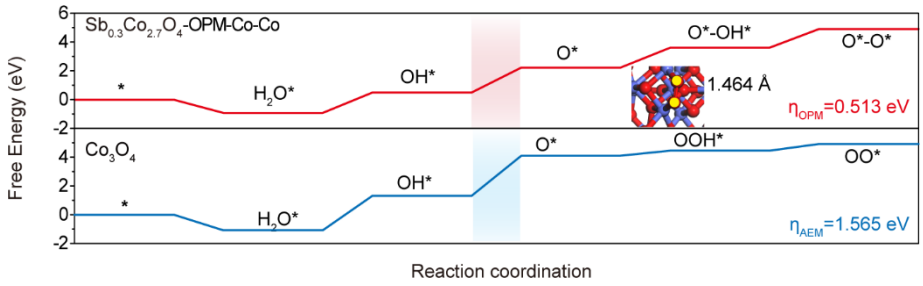

Figure S57. Gibbs free energy illustration for $Sb_{0.3}Co_{2.7}O_4$ and Co_3O_4 during OER by OPM and AEM pathways.

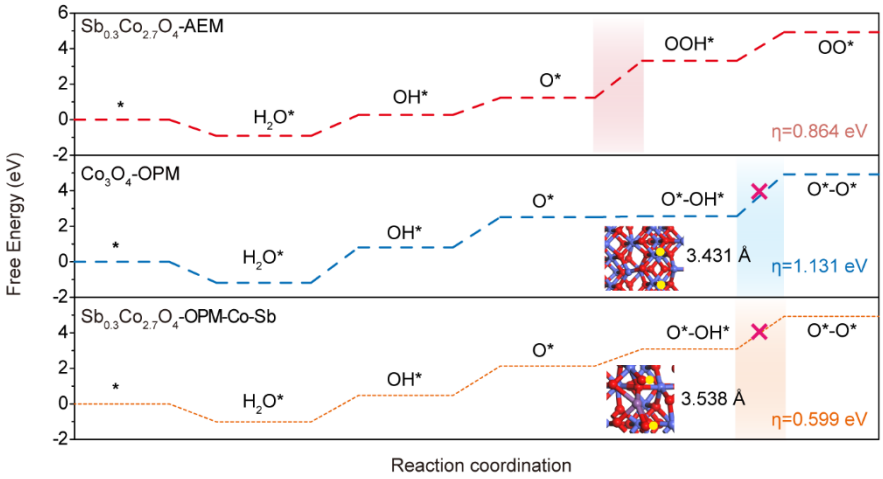

Figure S58. Gibbs free energy illustration for $Sb_{0.3}Co_{2.7}O_4$ and Co_3O_4 during OER by OPM and AEM pathways.

Firstly, as established in prior studies and confirmed by our HRTEM analysis (Figure 1b in the Manuscript), the (311) plane is the most thermodynamically stable surface for Co_3O_4 [6-7]. Consequently, we constructed slab models for both pristine Co_3O_4 (311) and $Sb_{0.3}Co_{2.7}O_4$ (311) (Figure S51). According to advanced literature, in the structure of spinel oxides (AB_2O_4), A-site cations occupy tetrahedrally coordinated centers, while B-site cations reside in octahedrally coordinated centers. Therefore, a key initial step is to determine whether Sb substitutes for Co at the A-site or the B-site (Figure S11). To theoretically validate the experimental finding from XAS that Sb adopts an octahedral doping configuration, we first considered two scenarios: Sb substituting for Co at octahedral sites and at tetrahedral sites. Building on this foundation, we constructed theoretical models of Co_3O_4 (311) with a Sb atom substituting at the tetrahedral and octahedral sites, respectively, and performed structural optimization. After full structural relaxation, as shown in Table S10, it was found that the model with substitution at the octahedral site exhibits lower energy, confirming that the octahedral doping configuration is more stable and thermodynamically favorable, which validates the experimental results of XAS.

Based on the above analysis, we further calculated the Gibbs free energies of various reaction pathways on $Sb_{0.3}Co_{2.7}O_4$ and Co_3O_4. DFT-calculated reaction pathways for $Sb_{0.3}Co_{2.7}O_4$ (via both AEM and OPM) and Co_3O_4 (via both AEM and OPM) are presented in Figures S52-S57. The rate-determining step (RDS) for the OPM pathway on $Sb_{0.3}Co_{2.7}O_4$ and AEM pathway on Co_3O_4 is the deprotonation of OH*. And the energy barrier of the RDS for the OPM pathway on $Sb_{0.3}Co_{2.7}O_4$ is 0.513 eV, significantly lower than that for AEM pathways on both $Sb_{0.3}Co_{2.7}O_4$ (0.864 eV) and Co_3O_4 (1.565 eV), indicating that the OPM mechanism was more likely to be triggered on

$Sb_{0.3}Co_{2.7}O_4$. More than this, to more rigorously verify the theoretical superiority of the OPM pathway on $Sb_{0.3}Co_{2.7}O_4$, we further compared the energy barriers of the OPM reaction pathway on $Sb_{0.3}Co_{2.7}O_4$ via the Co-Co dual sites and the Sb-Co dual sites, as well as on $Sb_{0.3}Co_{2.7}O_4$, as shown in Figure S58. The rate-determining step for both the OPM pathway on $Sb_{0.3}Co_{2.7}O_4$ via the Sb-Co dual sites and that on Co_3O_4 via the Co-Co dual sites is the step from O*-OH* to O*-O*, with energy barriers higher than that of the OPM pathway on $Sb_{0.3}Co_{2.7}O_4$ via the Co-Co dual sites. More importantly, based on the structure optimization results, the O*-O* coupling in these two cases is nearly unattainable. As illustrated in Figure S58, the optimized O*-O* distances in both scenarios significantly exceed the geometric requirements for realizing the OPM pathway.

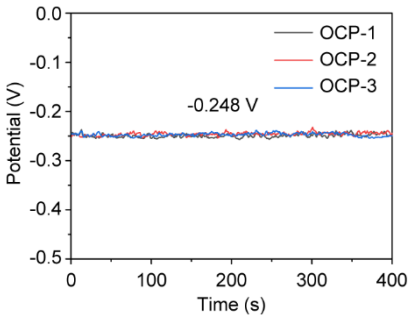

Figure S59. Time dependence of OCP of the Pt electrode in 0.5 M H_2SO_4 electrolyte.

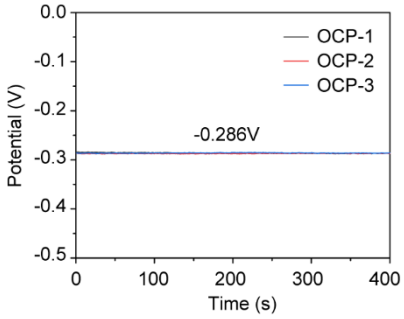

Figure S60. Time dependence of OCP of the Pt electrode in 0.5 M D_2SO_4 electrolyte.

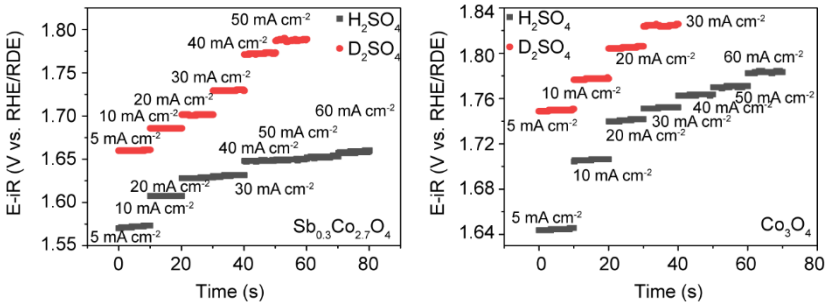

Figure S61. CA responses of Co_3O_4 and $Sb_{0.3}Co_{2.7}O_4$ measured in protic (H_2SO_4/H_2O) and deuterated (D_2SO_4/D_2O)

electrolytes.

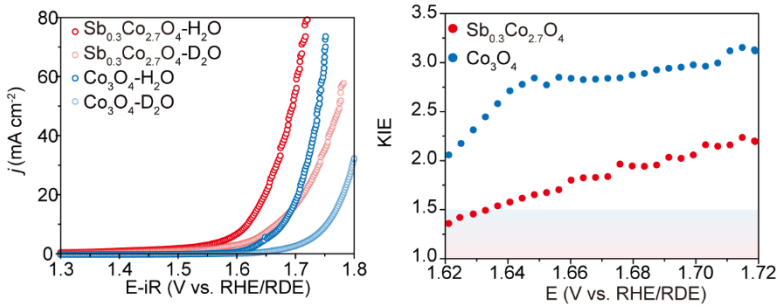

Figure S62. LSV curves of $Sb_{0.3}Co_{2.7}O_4$ and Co_3O_4 catalysts recorded in H_2SO_4 in H_2O solution vs. in 0.5 M H_2SO_4 in D_2O solution.

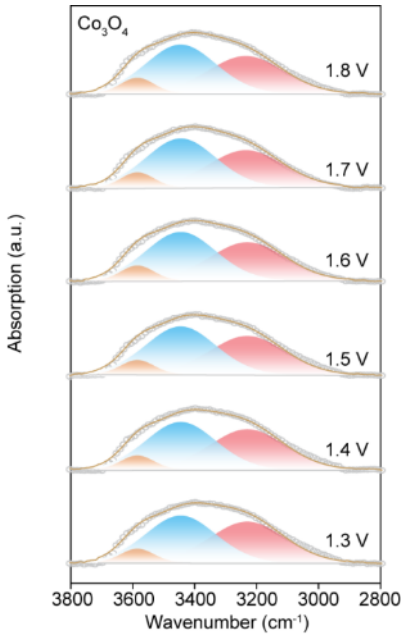

Figure S63. *In-situ* ATR-SEIRAS measurements of Co_3O_4 in the range of 2800 cm^{-1} to 3800 cm^{-1}.

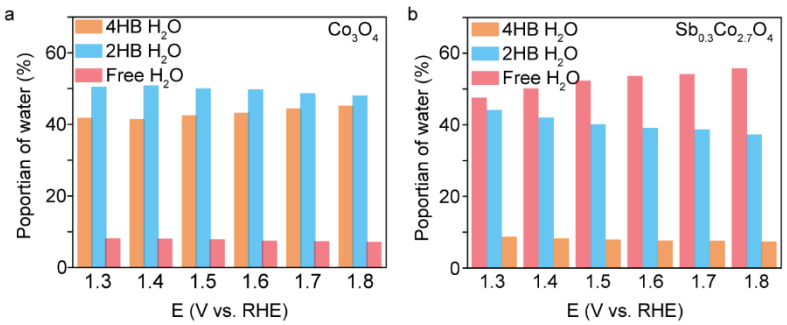

Figure S64. The proportions of 4HB H_2O 2HB H_2O and Free H_2O at varied potentials of (a) Co_3O_4 and (b) $Sb_{0.3}Co_{2.7}O_4$.

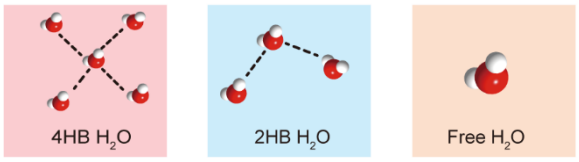

Figure S65. Schematic diagram of 4HB H_2O, 2HB H_2O and Free H_2O.

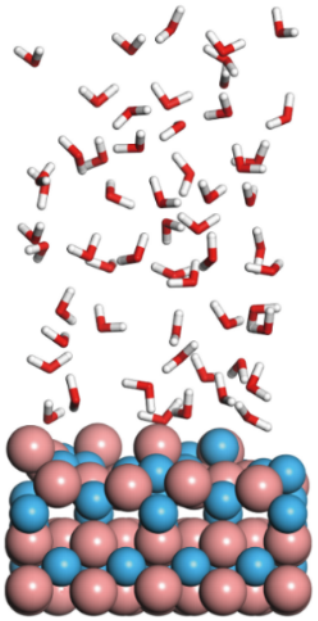

Figure S66. The representative snapshots of the structure of interfacial water molecules for Co_3O_4.

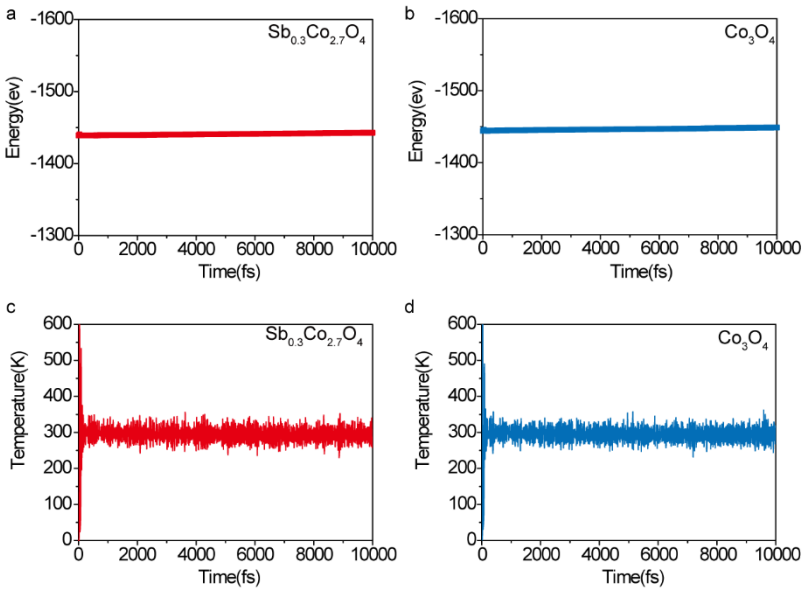

Figure S67. The evolution of temperature and energy during the 10000 fs AIMD simulation for $Sb_{0.3}Co_{2.7}O_4$ and Co_3O_4.

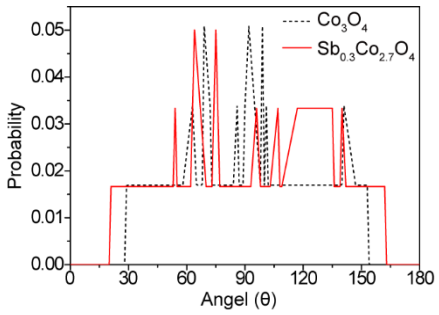

Figure S68. Angle distribution of interfacial water molecules orientation.

Table S1. ICP-AES results of Co_3O_4, $Sb_{0.4}Co_{2.6}O_4$, $Sb_{0.3}Co_{2.7}O_4$ and $Sb_{0.1}Co_{2.9}O_4$ (three experimental repeats).

Sample	Co（wt.%）	Co coefficient	Sb（wt.%）	Sb coefficient
$Sb_{0.4}Co_{2.6}O_4$	56.95 ± 0.76	2.56 ± 0.01	20.15 ± 0.42	0.44 ± 0.01
$Sb_{0.3}Co_{2.7}O_4$	67.76 ± 0.34	2.74 ± 0.03	13.39 ± 1.61	0.26 ± 0.03
$Sb_{0.1}Co_{2.9}O_4$	67.43 ± 1.37	2.94 ± 0.00	3.06 ± 0.09	0.06 ± 0.00
Co_3O_4	54.48 ± 0.39	~	~	~

Table S2. EDS quantitative analysis results of $Sb_{0.3}Co_{2.7}O_4$ at a 200 nm scale.

Element	Z	Family	Atomic Fraction (%)	Atomic error (%)
Co	27	K	90.72	1.09
Sb	51	L	9.28	1.09

Table S3. EDS quantitative analysis results of $Sb_{0.3}Co_{2.7}O_4$ at a 100 nm scale.

Element	Z	Family	Atomic Fraction (%)	Atomic error (%)
Co	27	K	90.14	0.76
Sb	51	L	9.86	0.76

Table S4. XPS results of $Sb_{0.3}Co_{2.7}O_4$ and Co_3O_4.

Samples	Peaks	Position (eV)	FWHM
Co_3O_4	I	779.68	1.38
	II	780.80	1.78
	III	781.96	1.97
	IV	785.78	4.25
	V	789.71	3.70
$Sb_{0.3}Co_{2.7}O_4$	I	779.68	1.39
	II	780.72	1.78
	III	781.98	2.18
	IV	785.78	4.30
	V	789.63	3.40

Table S5. EXAFS fitting parameters at the Co K-edge for various samples (S_0^2=0.67).

	shell	CN	R (Å)	σ^2	ΔE_0	R factor
Co foil	Co-Co	12,00	2.487 ± 0.002	0.00542	7.572	0.007
$Sb_{0.3}Co_{2.7}O_4$	Co-O	5.33 ± 0.50	1.904 ± 0.013	0.00372	7.990	0.006
	Co-O-Co_1	3.65 ± 0.25	2.843 ± 0.008	0.00300		
	Co-O-Co_2	9.55 ± 0.78	3.353 ± 0.009	0.01000		
Co_3O_4	Co-O	5.39 ± 0.62	1.946 ± 0.029	0.00335	1.270	0.011
	Co-O-Co_1	9.65 ± 2.33	2.900 ± 0.049	0.00830		
	Co-O-Co_2	4.47 ± 2.03	3.420 ± 0.073	0.00168		

Table S6. Mass activity of $Sb_{0.3}Co_{2.7}O_4$, Co_3O_4 and advanced non-noble metal-based catalysts.

Catalyst	Potential/ Overpotential	Mass activity (A g^{-1})	$Sb_{0.3}Co_{2.7}O_4$ (A g^{-1})	Co_3O_4 (A g^{-1})

$Mn_8O_{10}Br_3$	1.65 V	20.57[8]	71.74 ± 10.61	9.08 ± 1.65
Co_2TiO_4/CC	400 mV	~20[9]	45.43 ± 4.84	5.94 ± 1.22
CoCr	1.67 V	45[10]	121.25 ± 17.61	13.09 ± 2.01
Co_3O_4	386 mV	~19.5[11]	32.29 ± 1.13	4.44 ± 1.31
10%Ce-$NiCo_2O_4$	1.63 V	31.21[12]	45.43 ± 4.84	5.94 ± 1.22

Table S7. Comparison of the cell voltage and stability of our $Sb_{0.3}Co_{2.7}O_4$ with recently reported cobalt-based OER electrocatalysts in PEMWE.

Electrocatalyst	activity	Stability	Reference
$Sb_{0.3}Co_{2.7}O_4$	1 A cm^{-2}@2.01 V 2 A cm^{-2}@2.11 V	800 h@2 A cm^{-2}	This work
La/Mn-Co_3O_4	2 A cm^{-2}@2.47 V	100 h@210 mA cm^{-2}	[13]
$CoWO_4$(CWO-del-	1.8 A cm^{-2}@2 V	608 h@1 A cm^{-2}	[14]
ATO@17% CoHFe	6 mA cm^{-2}@1.8 V	22 h@~50 mA cm^{-2}	[15]
$Co_{1.8}Ga_{1.2}O_4$	200 mA cm^{-2}@1.75V	450 h@200 mA cm^{-2}	[16]
Ni(5%)Co_2MnO_4	1A cm^{-2} @ 2.3 V,	500 h@500 mA cm^{-2}	[17]
Nd-Co_3O_4	/	24 h@10 mA cm^{-2}	[11]
Ce-Mn-Co_3O_4/TiB_2	1A cm^{-2}@2.2 V	25 h@250 mA cm^{-2}	[18]
P-Co_3O_4	10 mA cm^{-2}@1.63V	30 h@10 mA cm^{-2}	[19]
V_o-Co_3O_4 HNC	1 A cm^{-2}@1.82V	~14 h@1 A cm^{-2}	[20]
Sn-Co_3O_4	160 mA cm^{-2}@2 V	120 h@100 mA/cm^{-2}	[21]

p-Co_3O_4	1 A cm^{-2}@1.85 V	/	[22]
CoCr	1.5 Acm^{-2}@2.17 V	500 h@0.1 A cm^{-2} 100 h@0.5 A cm^{-2}	[10]
$Co_3O_{4-x}F$	/	120 h@100 mA cm^{-2}	[23]
Na-Co_3O_4	0.1 A cm^{-2}@1.62 V 0.5 A cm^{-2}@2.1 V 1 A cm^{-2}@2.6 V	/	[24]
MoPr-Co_3O_4	/	110 h@100 mA cm^{-2}	[25]
Co-Co DASs/ZCC	50 mA cm^{-2}@1.5V	50 h@50 mA cm^{-2}	[26]
CoO/Co_3O_4	0.1 A cm^{-2} @1.78 V	160 h@100 mA cm^{-2}	[27]
Co-300	10 mA cm^{-2}@1.61 V	50 h@10 mA cm^{-2}	[28]
Co_3O_4/MnO_2	~250 mA cm^{-2}@1.7 V	10 h@~250 mA cm^{-2}	[29]

Table S8. Comparison of the stability of our $Sb_{0.3}Co_{2.7}O_4$ with recently reported Ru-based and Co-based OER electrocatalysts in PEMWE

Catalyst	**Activity**	**Stability**	**Membrane Type**	**Mass loading (mg cm^{-2})**	**Temperature (°C)**	**Reference**
i$Ga_{0.2}Ru_{0.8}O_2$	1.592 V (1 A cm^{-2})	200 h (0.5 A cm^{-2})	Hyproof HPM-2080X	-	80	[30]
Ru/MnO_2	1.71 V (1 A cm^{-2})	120 h (1 A cm^{-2})	N 115	5	60	[31]
C,Ta-RuO_2	1.63 V (1 A cm^{-2})	100 h (1 A cm^{-2})	N 115	1	60	[32]
Na/Hf-RuO_2	1.646 V (1 A cm^{-2})	85 h (0.5 A cm^{-2})	N 212	-	60	[33]
RuMnFeMoCo	1.85 V (1 A cm^{-2})	300 h (0.5 /1 A cm^{-2})	N 115	3	60	[34]

Catalyst	Activity	Stability	Membrane Type	Mass loading (mg cm^{-2})	Temperature (°C)	Reference
Co-Ru@RuO_2	1.58 V (1 A cm^{-2})	200 h (0.5 A cm^{-2})	N 115	0.5	60	[35]
Na-RuO_2	1.588 V (1 A cm^{-2})	25 h (0.5 A cm^{-2})	N 115	-	80	[36]
Ru_{MW}-$Mn_{1-x}Cr_xO_2$	1.88 V (1 A cm^{-2})	300 h (1 A cm^{-2})	N 115	2.5	80	[37]
Ta1/RuO_2	1.58 V (2 A cm^{-2})	650 h (0.5 A cm^{-2})	N 212	1.5	80	[38]
$Mn_{(SA)}$/RuO_2	1.78 V (1 A cm^{-2})	180 h (1A cm^{-2})	N 115/212	1.5	80	[39]
Bi-RuO_2 SAAO	1.58 V (1 A cm^{-2})	24 h (0.2A cm^{-2})	-	2	60	[40]
$Ru_{0.5}Mn_{0.5}O_2$	1.762 V (1 A cm^{-2})	120 h (0.5 A cm^{-2})	N 115	4	60	[41]
h-RuO_x	-	130 h (1A cm^{-2})	N 212	1.1	80	[42]
Ru-RuO_2-SN	1.6 V (1 A cm^{-2})	100 h (0.5 A·cm^{-2})	N 115	2	60	[43]
$Cr_{0.6}Ru_{0.4}O_2$	1.537 V (1 A cm^{-2}) 1.765 V (2 A cm^{-2})	350 h (0.3 A cm^{-2})	N 212	1	60	[44]
RuO_2/MoO_3-SO_4	1.75 V (1 A cm^{-2})	150 h (0.5 A cm^{-2})	N 115	2	50	[45]
PtRu-Co_3O_4	1.83 V (1 A cm^{-2})	200 h (0.2 A cm^{-2})	N 115	~4	50	[46]
LD-B/RuO_2	1.63 V (1 A cm^{-2})	300 h (0.25 A cm^{-2})	N 117	~2	80	[47]
$Cr_{0.2}Ru_{0.8}O_{2-x}$	1.77 V (1 A cm^{-2})	200 h (1 A cm^{-2})	N 115	~3	60	[48]

Catalyst	Activity	Stability	Membrane Type	Mass loading (mg cm^{-2})	Temperature (°C)	Reference
Pb-RuO_2	1.688 V (1 A cm^{-2})	100 h (1 A cm^{-2})	N 212	1	-	[49]
$InSnRuO_2$	1.66 V (1 A cm^{-2})	200 h (0.05 A cm^{-2})	N 115	0.3	60	[50]
Ru(SA)-NiOMS	2.15 V (1 A cm^{-2})	100 h (0.5 A cm^{-2})	-	-	25	[51]
$RuCo/RuCoO_x$	1.784 V (1 A cm^{-2})	200 h (0.2 A cm^{-2})	N 115	5	80	[52]
$RuTiO_x$	1.54 V (1 A cm^{-2})	100 h (0.5 A cm^{-2})	N 117	1	40	[53]
$Mn_{0.2}Ru_{0.8}O_2$	1.8 V (3.15 A cm^{-2})	100 h (0.2 A cm^{-2})	N 212	2	80	[54]
ZrO_2-RuO_2	1.68 V (1 A cm^{-2})	100 h (2 A cm^{-2})	N 117	2.5	80	[55]
Er-RuO_x	1.59 V (1 A cm^{-2})	100 h (1 A cm^{-2})	N 117	3	80	[56]
$(Ru–W)O_x$	1.62 V (1 A cm^{-2})	50 h (1 A cm^{-2})	N 117	2	80	[57]
Sm-$MnCo_2O_{4.5}$	1.73 V (0.5 A cm^{-2})	300 h (0.5 A cm^{-2})	N 117	2.5	80	[58]
Nd-CoO_x	1.93V (1 A cm^{-2})	100 h (0.2 A cm^{-2})	N 117	5	80	[59]
CoOOH	2.36 V (2 A cm^{-2})	400 h (0.1 A cm^{-2})	N 212	2	80	[60]
$[Co-Fe-Pb]O_x$	-	460 h (1 A cm^{-2})	-	-	80	[61]
c-Co_3O_4@NFs	1.7 V (0.25 A cm^{-2})	200 h (0.1 A cm^{-2})	N 115	2	80	[62]

Catalyst	Activity	Stability	Membrane Type	Mass loading (mg cm^{-2})	Temperature (°C)	Reference
La/Mn-Co_3O_4	2.47 V (2 A cm^{-2})	100 h (0.21 A cm^{-2})	N 212	1-2	80	[14]
CWO-del-48	2 V (1.8 A cm^{-2})	608 h (1 A cm^{-2})	N 117	4	80	[15]
$Co_3O_{4-x}F$	-	120 h (0.1 A cm^{-2})	N 117	~3	50	[29]
W-Co_3O_4	1.83 V (1 A cm^{-2})	240 h (1 A cm^{-2})	N 115	8	50	[63]
Co_3O_4/MnO_2	1.7 V (~0.25 A cm^{-2})	10 h (~0.25 A cm^{-2})	-	-	-	[23]
ATO@17% CoHFe	1.8 V (0.006 A·cm^{-2})	22 h (~0.05 A·cm^{-2})	-	-	80	[64]
Ni(5%)Co_2MnO_4	2.3 V (1 A·cm^{-2})	500 h (0.5 A·cm^{-2})	N 117	4	80	[17]
Nd-Co_3O_4	-	24 h (0.01 A cm^{-2})	-	-	-	[11]
Ce-Mn-Co_3O_4/TiB_2	2.2 V (1 A·cm^{-2})	25 h (0.25 A·cm^{-2})	N 117	-	-	[18]
P-Co_3O_4	-	30 h (0.01 A cm^{-2})	-	-	-	[19]
V_o-Co_3O_4 HNC	1.82 V (1 A cm^{-2})	~14 h (1 A cm^{-2})	-	2	80	[20]
Sn-Co_3O_4	2 V (0.16 A cm^{-2})	120 h (0.1 A cm^{-2})	N117	-	80	[21]
CoCr	2.17 V (1.5 A cm^{-2})	100 h (0.5 A cm^{-2})	N212	4.8	80	[10]
Na-Co_3O_4	2.6 V (1 A·cm^{-2})	-	-	-	-	[24]

Catalyst	Activity	Stability	Membrane Type	Mass loading (mg cm^{-2})	Temperature (°C)	Reference
MoPr-Co_3O_4	-	110 h (0.1 A cm^{-2})	-	-	80	[25]
Zr-Co_9S_8/Co_3O_4	-	50 h (0.05 A cm^{-2})	N117	5	80	[65]
CoO/Co_3O_4	1.78 V (0.1 A cm^{-2})	160 h (0.1 A cm^{-2})	N117	-	80	[27]

Table S9. EXAFS fitting parameters at the Co K-edge for various samples (S_0^2=0.67).

	shell	CN	R (Å)	σ^2	ΔE_0	R factor
Co foil	Co-Co	12.00	2.487 ± 0.002	0.00542	7.572	0.007
$Sb_{0.3}Co_{2.7}O_4$ -OCP	Co-O	5.20 ± 1.69	1.906 ± 0.011	0.00703	6.966	0.001
	Co-O-Co_1	3.65 ± 0.25	2.826 ± 0.026	0.00479		
	Co-O-Co_2	0.83 ± 1.10	3.310 ± 0.030	0.01794		
$Sb_{0.3}Co_{2.7}O_4$ -1.7 V	Co-O	5.24 ± 1.22	1.897 ± 0.020	0.00393	4.011	0.007
	Co-O-Co_1	3.22 ± 0.31	2.842 ± 0.026	0.00967		
	Co-O-Co_2	1.56 ± 0.32	3.329 ± 0.014	0.01763		
Co_3O_4 -OCP	Co-O	4.99 ± 0.79	1.920 ± 0.003	0.00217	4.803	0.012
	Co-O-Co_1	8.40 ± 3.24	2.860 ± 0.011	0.00790		
	Co-O-Co_2	8.98 ± 5.46	3.380 ± 0.037	0.00777		
Co_3O_4 -1.6 V	Co-O	3.97 ± 0.78	1.931 ± 0.014	0.00027	2.77	0.007
	Co-O-Co_1	10.62 ± 4.95	2.890 ± 0.038	0.01028		
	Co-O-Co_2	5.54 ± 5.16	3.390 ± 0.041	0.00513		

Table S10. Final energy of three slabs after structural relaxation.

Samples	Final Energy（eV）
$Sb_{0.3}Co_{2.7}O_4$-Oh	-116049.9622
$Sb_{0.3}Co_{2.7}O_4$-Td	-116048.7921
Co_3O_4	-116940.2952

REFERENCES

1. M. C. Biesinger, B. P. Payne, A. P. Grosvenor, L. W. M. Lau, A. R. Gerson and R. S. C. Smart, *Appl. Surf. Sci.*, 2011, **257**, 2717–2730.
2. H. Ding, Y. Long, J. Shen and M. Wan, *J. Phys. Chem. B*, 2010, **114**, 115–119.
3. S. She, C. Chen, K. Fan, G. Chen, Y. Zhu, D. Guan, Y.-C. Huang, H.-C. Chen, Z. Lin, H. F. Wong, L. Li, Y. Zhu, C. W. Leung, Y. H. Tsang and H. Huang, *J. Am. Chem. Soc.*, 2025, **147**, 24392–24402.
4. X. Wang, W. Pi, Z. Li, S. Hu, H. Bao, W. Xu and N. Yao, *Nat. Commun.*, 2025, **16**.
5. L. Wu, W. Huang, D. Li, B. Zhao, H. Zhou and W. Luo, *Angew. Chem., Int. Ed.*, 2025, **64**, e202420848.
6. Y. Hao, S.-F. Hung, W.-J. Zeng, Y. Wang, C. Zhang, C.-H. Kuo, L. Wang, S. Zhao, Y. Zhang, H.-Y. Chen and S. Peng, *J. Am. Chem. Soc.*, 2023, **145**, 23659–23669.
7. J. Liu, V. Fung, Y. Wang, K. Du, S. Zhang, L. Nguyen, Y. Tang, J. Fan, D.-e. Jiang and F. F. Tao, *Applied Catalysis B: Environmental*, 2018, **237**, 957–969.
8. S. Pan, H. Li, D. Liu, R. Huang, X. Pan, D. Ren, J. Li, M. Shakouri, Q. Zhang, M. Wang, C. Wei, L. Mai, B. Zhang, Y. Zhao, Z. Wang, M. Graetzel and X. Zhang, *Nat. Commun.*, 2022, **13**. 2294.
9. S. Anantharaj, K. Karthick and S. Kundu, *Inorg. Chem.*, 2019, **58**, 8570–8576.
10. Q. Yan, J. Feng, W. Shi, W. Niu, Z. Lu, K. Sun, X. Yang, L. Xue, Y. Liu, Y. Li and B. Zhang, *Advanced Science*, 2024, **11**, 202402356.
11. X. Zhang, M. Zhang, S. Zhang, T. S. Baizhumanova, S. A. Tungatarova, H. Zhang, C. Chen, Y. Han, X. Li and S. Ma, *J. Alloys Compd.*, 2025, **1031**, 181103.
12. Y. Li, H. Cheng, J. Zhang and Y. Fu, *Appl. Surf. Sci.*, 2026, **717**, 164784.
13. L. Chong, G. Gao, J. Wen, H. Li, H. Xu, Z. Green, J. D. Sugar, A. J. Kropf, W. Xu, X.-M. Lin, H. Xu, L.-W. Wang and D.-J. Liu, *Science*, 2023, **380**, 609–616.
14. R. Ram, L. Xia, H. Benzidi, A. Guha, V. Golovanova, A. G. Manjón, D. L. Rauret, P. S. Berman, M. Dimitropoulos, B. Mundet, E. Pastor, V. Celorrio, C. A. Mesa, A. M. Das, A. Pinilla-Sánchez, S. Giménez, J. Arbiol, N. López and F. P. G. d. Arquer, *Science*, 2024, **384**, 1373–1380
15. X. Xu, H. Sun, S. P. Jiang and Z. Shao, *SusMat*, 2021, **1**, 460–481.
16. D. Zhou, J. Yu, J. Tang, X. Y. Li and P. Ou, *Adv. Energy Mater.*, 2024, **15**, 2404007.
17. C. W. Lee, C. Cazorla, S. Zhou, D. Zhang, H. Xu, W. Zhong, M. Zhang, D. Chu, Z. Han and R. Amal, *Adv. Energy Mater.*, 2024, **15**, 2402786.
18. Z. Wang, J. Li, C. Wang, J. Wang, X. Chen, J. Wu, Z. Bai, Y. Gao, L. Chen and X. Yan, *Mater. Today Phys.*, 2025, **51**, 101641.
19. F. Shang, H. He, P. Li, H. Cai, B. An, X. Li, S. Yang, Z. Sun and B. Wang, *Colloid. Interface Sci.*, 2023, **641**, 329–337.
20. C. Rong, S. Wang, X. Shen, C. Jia, Q. Sun, Q. Zhang and C. Zhao, *Energy Environ. Sci.*, 2024, **17**, 4196–4204.
21. L.-Y. Chueh, Y.-W. Hsu, Z.-W. Wang, H.-C. Lin, S.-Y. Hung, Y.-L. Chen, H.-Y. Chen and Y.-T. Pan, *Electrochim. Acta*, 2024, **497**, 144575.
22. M. Cui, R. Guo, Y. Zhou, W. Zhao, Y. Liu, W. Luo, Q. Ou and S. Zhang, *ACS Catal.*, 2024, **14**, 16353–16362.
23. Y. Wang, P. Guo, J. Zhou, B. Bai, Y. Li, M. Li, P. Das, X. Wu, L. Zhang, Y. Cui, J. Xiao and Z.-S. Wu, *Energy Environ. Sci.*, 2024, **17**, 8820–8828.
24. P. Huang, X. Feng, C. Zhou, X. Xu, G. Wang, H. Hu and F. Hu, *Chem. Eng. J.*, 2024, **500**, 156846.
25. W. Wu, B. Liu, X. Xu, P. Jing, L. Li and J. Zhang, *Inorg. Chem.*, 2025, **64**, 12174–12188.
26. L. Wang, H. Su, Z. Zhang, J. Xin, H. Liu, X. Wang, C. Yang, X. Liang, S. Wang, H. Liu, Y. Yin, T. Zhang, Y. Tian, Y. Li, Q. Liu, X. Sun, J. Sun, D. Wang and Y. Li, *Angew. Chem., Int. Ed.*, 2023, **62**, e202314185
27. D. Zhang, D. Zhang, Y. Cao, Y. Chen and B. Liu, *ACS Appl. Nano Mater.*, 2025, **8**, 6615–6625.
28. Q. Lai, V. Vediyappan, K.-F. Aguey-Zinsou and H. Matsumoto, *ADV ENERG SUST RES*, 2021, **2**, 2100086.

29. J. Wang, Y. Zhang, Y. Wang, J. Cho, T.-S. Chan, Y. Ha, S.-C. Haw, C.-W. Kao, Z. Wang, J. Lei, M. Ju, J. Tang, T. Liu, S. Zhao, Y. Dai, A. Baron-Wiechec, F.-R. Chen, W. Wang, C. H. Choi, Z. Shao and M. Ni, *Energy Environ. Sci.*, 2024, **17**, 5972–5983.
30. H. Wang, C. Lin, L. Tan, J. Shen, X. Wu, X. Pan, Y. Zhao, H. Zhang, Y. Sun, B. Mei, H.-D. Um, Q. Xiao, W. Jiang, X. Li and W. Luo, *Nat. Commun.*, 2025, **16**, 3976.
31. M. Qi, X. Du, X. Shi, S. Wang, B. Lu, J. Chen, S. Mao, H. Zhang and Y. Wang, *J. Am. Chem. Soc.*, 2025, **147**, 18295–18306.
32. X. Jiang, J. Zhu, M. Jiang, P. Zhang, W. Wen, W. Cai, Y. Ding, P. Sun and M. Cao, *Adv. Mater.*, 2025, **37**, 202503354.
33. Y. a. Zhu, F. Wu, X. Zhang, Y. Lin, L. Zhang, T. S. Chan, Q. Zhang and L. Chen, *Adv. Mater.*, 2025, **37**, 2500449.
34. J. Chen, J. Ma, T. Huang, Q. Liu, X. Liu, R. Luo, J. Xu, X. Wang, T. Jiang, H. Liu, Z. Lv, T. Yao, G. Wang, X. Zheng, Z. Li and W. Chen, *Angew. Chem., Int. Ed.*, 2025, **64**, e202503330
35. J. Chen, Y. Ma, C. Cheng, T. Huang, R. Luo, J. Xu, X. Wang, T. Jiang, H. Liu, S. Liu, T. Huang, L. Zhang and W. Chen, *J. Am. Chem. Soc.*, 2025, **147**, 8720–8731.
36. W. Li, D. Chen, Z. Lou, H. Yuan, X. Fu, H. Y. Lin, M. Lin, Y. Hou, H. Qi, P. F. Liu, H. G. Yang and H. Wang, *J. Am. Chem. Soc.*, 2025, **147**, 10446–10458.
37. Y. Shi, L. Wang, M. Liu, Z. Xu, P. Huang, L. Liu and Y. Xu, *Nat. Commun.*, 2025, **16**, 909.
38. J. Shim, K. Lee, Y. Yu, H. S. Lee, H. Shin, K.-S. Lee, M. S. Bootharaju, S. Han, G. S. Yi, H. Ko, S. Lee, J. Ryu, M. Kim, B.-H. Lee, T. Hyeon and Y.-E. Sung, *J. Am. Chem. Soc.*, 2025, **147**, 16179–16188.
39. Z.-H. Xue, J. Mahmood, Y. Shang, G. Li, S.-J. Kim, Y. Han and C. T. Yavuz, *J. Am. Chem. Soc.*, 2025, **147**, 17839–17848.
40. Z. Yang, Y. Ding, W. Chen, S. Luo, D. Cao, X. Long, L. Xie, X. Zhou, X. Cai, K. Liu, X. Z. Fu and J. L. Luo, *Adv. Mater.*, 2025, **37**, 202417777.
41. Y. Liu, X. Li, H. Jang, J. Wu, M. G. Kim, X. Xi, Z. Lei, Y. Zhang, Y. Deng, W. Yan, J. Jiang, S. Jiao, J.-L. Luo and R. Cao, *Energy Environ. Sci.*, 2025, **18**, 3352–3364.
42. J. Tang, D. Guan, H. Xu, L. Zhao, U. Arshad, Z. Fang, T. Zhu, M. Kim, C.-W. Pao, Z. Hu, J. Ge and Z. Shao, *Nat. Commun.*, 2025, **16**, 801.
43. Y. Song, W. Zhao, Z. Wang, W. Shi, F. Zhang, Z. Wei, X. Cui, Y. Zhu, T. Wang, L. Sun and B. Zhang, *J. Am. Chem. Soc.*, 2025, **147**, 13775–13783.
44. X. Cao, H. Qin, J. Zhang, X. Chen and L. Jiao, *J. Am. Chem. Soc.*, 2024, **146**, 32049-32058.
45. Y. Duan, L. L. Wang, W. X. Zheng, X. L. Zhang, X. R. Wang, G. J. Feng, Z. Y. Yu and T. B. Lu, *Angew. Chem., Int. Ed.*, 2024, **63**, e202413653.
46. D. Li, D. Xu, Y. Pei, Q. Zhang, Y. Lu and B. Zhang, *J. Am. Chem. Soc.*, 2024, **146**, 28728–28738.
47. G. Chen, R. Lu, C. Ma, X. Zhang, Z. Wang, Y. Xiong and Y. Han, *Angew. Chem., Int. Ed.*, 2024, **63**, e202411603.
48. Y. Shen, X.-L. Zhang, M.-R. Qu, J. Ma, S. Zhu, Y.-L. Min, M.-R. Gao and S.-H. Yu, *Nat. Commun.*, 2024, **15**, 7861.
49. C. Zhou, L. Li, Z. Dong, F. Lv, H. Guo, K. Wang, M. Li, Z. Qian, N. Ye, Z. Lin, M. Luo and S. Guo, *Nat. Commun.*, 2024, **15**, 9774.
50. Y. Sun, M. Xiao, F. Liu, J. Gan, S. Gao and J. Liu, *Adv. Mater.*, 2024, **36**, 2414579.
51. Y. Hao, S.-F. Hung, L. Wang, L. Deng, W.-J. Zeng, C. Zhang, Z.-Y. Lin, C.-H. Kuo, Y. Wang, Y. Zhang, H.-Y. Chen, F. Hu, L. Li and S. Peng, *Nat. Commun.*, 2024, **15**, 8015.
52. W. Hu, B. Huang, M. Sun, J. Du, Y. Hai, W. Yin, X. Wang, W. Gao, C. Zhao, Y. Yue, Z. Li and C. Li, *Adv. Mater.*, 2024, **37**, 2411709.
53 H. Jun, E. Kang, J. Moon, H. Kim, S. Han, S. Choung, S. Kim, S. Y. Yi, E. Kang, C. H. Choi, J. W. Han and J. Lee, *Chem*, 2025, **11**, 102367.

54 L. Deng, H. Chen, S.-F. Hung, Y. Zhang, H. Yu, H.-Y. Chen, L. Li and S. Peng, *J. Am. Chem. Soc.*, 2024, **146**, 35438–35448.

55 L. Li, G. Zhang, C. Zhou, F. Lv, Y. Tan, Y. Han, H. Luo, D. Wang, Y. Liu, C. Shang, L. Zeng, Q. Huang, R. Zeng, N. Ye, M. Luo and S. Guo, *Nat. Commun.*, 2024, **15**, 4974.

56 L. Deng, S. F. Hung, Z. Y. Lin, Y. Zhang, C. Zhang, Y. Hao, S. Liu, C. H. Kuo, H. Y. Chen, J. Peng, J. Wang and S. Peng, *Adv. Mater.*, 2023, **35**, 202305939.

57 M. Li, J. Yang, S. Li, L. Deng, S. Zhao, L. Li, S.-F. Hung, G. Xing, T. Wang, Y. Liang, J. Ren, Y. Wu and S. Peng, *J. Am. Chem. Soc.*, 2025, **147**, 45680–45690.

58 L. Wu, B. Zhao, W. Huang, D. Li, Z. Liao, Y. Chen, N. Yao, H. Zhou and W. Luo, *Nat. Commun.*, 2026, **17**, 2598.

59 Y. Feng, J. Wang, K. Feng, B. Xu, J. Xu, S. Li, C. Lu, X. Fan, H. Lin and J. Zhong, *Nat. Commun.*, 2025, **16**, 10998.

60 J. Huang, Z. Zhang, C. Spezzati, A. H. Clark, N. Hales, N. S. Genz, N. Daffé, R. Skoupy, L. Gubler, I. E. Castelli, T. J. Schmidt and E. Fabbri, *Nat. Commun.*, 2025, **16**, 7518.

61 D. Simondson, M. F. Tesch, I. Spanos, T. E. Jones, J. Guo, B. V. Kerr, M. Chatti, S. A. Bonke, R. Golnak, B. Johannessen, J. Xiao, D. R. MacFarlane, R. K. Hocking and A. N. Simonov, *Nat. Energy*, 2025, **10**, 1013–1024.

62 Y. Tang, N. N. Liang, Y. Li, Q. Luo, W. Ding, B. Li, X. Gao, Q. Pang, D. Ji and M. Luo, *Adv. Energy Mat.*, 2026, DOI:10.1002/aenm.202506692, 202506692.

63 J. Cao, D. Zhang, B. Ren, P. Song and W. Xu, *Energy Environ. Sci.*, 2024, **17**, 59115921.

64 B. Rodríguez-García, Á. Reyes-Carmona, I. Jiménez-Morales, M. Blasco-Ahicart, S. Cavaliere, M. Dupont, D. Jones, J. Rozière, J. R. Galán-Mascarós and F. Jaouen, *Sustainable Energy & Fuels*, 2018, **2**, 589–597.

65 L. Wang, H. Su, Z. Zhang, J. Xin, H. Liu, X. Wang, C. Yang, X. Liang, S. Wang, H. Liu, Y. Yin, T. Zhang, Y. Tian, Y. Li, Q. Liu, X. Sun, J. Sun, D. Wang and Y. Li, *Angew. Chem., Int. Ed.*, 2023, **62**, e202314185